Transport Phenomena Across Interfaces of Complex Fluids: Drops and Sprays

Volfango Bertola and Günter Brenn

Abstract This chapter gives an overview of the interfacial dynamics of complex fluids, with focus on non-Newtonian drop impact phenomena and non-Newtonian sprays. After a general introduction about Newtonian drops and sprays, the impact dynamics of viscoelastic and viscoplastic drops on both homothermal and heated surfaces is discussed. Finally, capillary instabilities and the atomisation process of non-Newtonian fluids are described.

1 Introduction

Since the pioneering works of Plateau (1867), Worthington (1876) and Rayleigh (1879), drop impact phenomena and liquid atomisation processes have been the subject of extensive investigations, which had a huge impact on several industrial and everyday applications, from spray cleaning or painting to internal combustion engines, and so on.

The morphology of drop impact on solid surfaces is well known (Rein 1993; Yarin 2006; Josserand and Thoroddsen 2016). Upon impact, the liquid spreads on the surface taking the form of a disc; for low impact velocity, the disc thickness is approximately uniform, while for higher impact velocities, the disc is composed of a thin central part, the so-called *lamella*, surrounded by a toroidal rim. This initial spreading stage is typically very fast and has a duration of about 5 ms. After the drop has reached maximum spreading, two qualitatively different outcomes are possible. If the initial kinetic energy exceeds a threshold value, capillary forces are insufficient to maintain the integrity of the drop, which disintegrates into smaller satellite droplets jetting out of its outermost perimeter; this phenomenon is usually referred to as

V. Bertola (✉)
School of Engineering, University of Liverpool, Liverpool, UK
e-mail: Volfango.Bertola@liverpool.ac.uk

G. Brenn
Institut für Strömungslehre und Wärmeübertragung, Technische Universität Graz, Graz, Austria

T. Burghelea and V. Bertola (eds.), *Transport Phenomena in Complex Fluids*,
CISM International Centre for Mechanical Sciences 598,
https://doi.org/10.1007/978-3-030-35558-6_7

splashing, or less frequently as *drop breakup*. If splashing does not occur, the drop is allowed to retract under the action of capillary forces, which tend to minimise the contact with the surface; in some cases, retraction is so fast that the liquid rises in the middle forming a Worthington jet, which may subsequently result in the complete rebound of the drop.

Impacts onto smooth and chemically homogeneous surfaces, for low or moderate impact kinetic energy, are controlled by three key factors: inertia, viscous dissipation and interfacial energy. During the initial stages of impact with the surface, the vertical inertia of the falling drop is converted into the horizontal motion of the fluid, and as the drop spreads, kinetic energy is partially stored as surface energy. This process is characterised by the Weber number, $We = \rho U^2 D_0/\sigma$, where ρ and σ are the fluid density and surface tension, respectively, D_0 is the equilibrium drop diameter and U is the normal impact velocity. As the fluid spreads across the surface, the kinetic energy of the fluid is partly dissipated by viscous forces in the fluid, which is described using the Reynolds number, $Re = \rho U D_0/\mu$, where μ is the fluid viscosity; this is sometimes used in combination with the Weber number to yield the Ohnesorge number, $Oh = \sqrt{We}/Re$. Finally, the retraction stage is governed by the balance between interfacial energy and viscous dissipation, expressed by the Capillary number, $Ca = \mu U_r/\sigma$, where U_r is the retraction velocity.

Thus, the spreading behaviour of impacting drops is mainly characterised by the Weber and by the Ohnesorge numbers, which portray the driving and the resisting/dissipative forces of the process, respectively. The corresponding asymptotic spreading behaviours are (Schiaffino and Sonin 1997) as follows:

- High We, low Oh (inviscid, impact-driven). The spreading is primarily driven by dynamic pressure. The characteristic time scale of the inertial spreading is very short. Viscous effects are negligible during the initial stage of spreading, however damp the subsequent drop oscillations.
- Low We, low Oh (inviscid, capillarity-driven). The spreading is mainly driven by the capillary forces at the contact line and the impact velocity effects are negligible. Spreading is followed by interfacial oscillations with the timescale of the same order as the spreading.
- Low We, high Oh (highly viscous, capillarity-driven). The spreading is driven by capillary forces and resisted by viscous forces. Impact velocity has negligible effects. The inertial oscillations are overdamped by high viscosity.
- High We, high Oh (highly viscous, impact-driven). The spreading is driven by inertial forces and resisted by viscous forces. Capillarity has negligible effects. Drop oscillations are absent.

There are a number of empirical, semi-empirical and theoretical models to predict the maximum diameter of the drop, D_m, at the end of the inertial spreading stage. These models are based either on scaling considerations (Clanet et al. 2004) or, more frequently, on the energy balance, which can be written as follows:

$$\frac{d}{dt}(E_k + E_g + E_s) + \dot{W} = 0 \tag{1}$$

where E_k denotes the kinetic energy of the drop, E_g is the gravity potential energy, E_s is the surface energy, $\dot{W}$ is the rate of total energy loss during drop impact, including viscous dissipation and the energy transmitted to the substrate due to deformation. However, the energy absorbed by the substrate is often neglected and only the viscous dissipation is considered for the energy loss rate. The viscous dissipation is the most difficult quantity to estimate precisely due to the limited information about the flow field inside the drop. Another difficult quantity to estimate is surface energy, because the precise calculation of the surface energy at the end of spreading strongly depends on the shape of the liquid free surface. In particular, if the drop shape at maximum spreading is approximated as a disc (Ford and Furmidge 1967) its surface energy can be written as follows:

$$E_s = \frac{\pi}{4} D_m^2 \sigma (1 - cos\theta_a) = 0 \tag{2}$$

where θ_a is the advancing contact angle; if the drop shape is approximated as a spherical cap (Bechtel et al. 1981), the surface energy is

$$E_s = \frac{\pi}{3} D_0^2 \sigma [\xi_m^{-1} + 2\xi_m^2 - (\xi_m^{-1} - \xi_m^2) cos\theta_s] = 0 \tag{3}$$

where θ_s is the static contact angle and $\xi_m = h_{\min}/D_0$ is the minimum height factor.

Models based on the energy conservation approach were proposed, among others, by Bechtel et al. (1981), Chandra and Avedisian (1991), Pasandideh-Fard et al. (1996), Mao et al. (1997), Attané et al. (2007). However, although these models give reasonably accurate predictions in case of low-viscosity fluids, they almost systematically fail when the importance of the viscous dissipation term is increased (German and Bertola 2009b).

More recently, the analytical self-similar solution which satisfies the full Navier–Stokes equations was obtained for the viscous flow in the spreading drop (Roisman et al. 2009; Roisman 2009). The boundary layer thickness was used for the estimation of the residual film thickness formed by normal drop impact and the maximum spreading diameter. A very similar approach was later used by Eggers et al. (2010) to obtain equivalent results.

Drop splashing occurs as the inertial forces overcome those due to capillarity, expressed by the Laplace pressure:

$$\rho U_0^2 > \frac{\sigma h_L}{D_0^2} \tag{4}$$

where h_L is the thickness of the lamella. When Eq. (4) is re-formulated in terms of dimensionless numbers, the splashing criterion can be written as $\alpha Oh^\beta We^\gamma > K$ (Stow and Hadfield 1981; Mundo et al. 1995), where α, β, γ and K are constants. A comprehensive review of existing splashing correlations is reported by Moreira et al. (2010), while basic hydrodynamic modelling is discussed by Yarin (2006).

When the target surface is heated, the drop impact phenomenology is characterised by a close interplay of hydrodynamics with different heat transfer modes, under large spatial and temporal gradients of the state variables (Rein 2003). Early studies of these phenomena focused on the heat transfer characteristics (Wachters and Westerling 1966; Gottfried et al. 1966), and less attention was paid to drop impact morphology due to the limitations of stroboscopic imaging (Pedersen 1970). Later on, the development of high-speed imaging allowed researchers to visualise and analyse more quantitatively the various impact regimes, and to get a deeper insight into the physical mechanisms behind different impact outcomes (Fujimoto et al. 2010).

After impact, the drop spreads on the heated surface in a short lapse of time (typically a few milliseconds in case of drops of millimetric size), increasing the area exposed to heat transfer. This induces a heat transfer regime that can be related to the well-known boiling curve, in particular, one can observe: (i) convection heat transfer for surface temperatures below the boiling point of the liquid; (ii) nucleate boiling for surface temperatures just above the boiling point; (iii) film boiling, observed above the critical heat flux (CHF), where the drop is separated from the surface by a vapour layer and (iv) transitional boiling, where the said vapour layer is unstable and the liquid may locally get into contact with the surface. However, the association between heat transfer and impact regimes is not always clear (Wang et al. (2000)).

The classification of impact regimes, reviewed by Moreira et al. (2010), is still somewhat controversial. To rationalise the rich variety of impact morphologies observed for Newtonian drops impinging on heated surfaces, it was proposed to identify *simple* impact regimes, displaying one distinctive feature (deposition, rebound, splashing/breakup) and *mixed* regimes, resulting from the combination of simple regimes with secondary atomisation (Bertola 2015), as shown in Fig. 1. Such unifying classification, on one hand, embraces the different impact morphologies reported in the existing literature, and on the other hand is simple enough to be used for practical purposes; in addition, it allows one to derive simple models for transition boundaries between different impact regimes.

The breakup of a liquid jet into smaller droplet is another process of fundamental importance, because it maximises the free surface of a given volume of liquid, increasing significantly mass, momentum and heat transfer rates, as well as chemical reaction rates, between the fluid and a surrounding medium. Observing the decay of fluid jets travelling through a medium of the same density, Plateau (1867) recognised that perturbations would become unstable if their wavelength λ was greater than a critical value $\lambda_{cr}/R_0 = 2\pi$, where R_0 is the capillary tube radius; however, the wavelength corresponding to the fastest breakup was $\lambda_{cr}/R_0 = 8.76$, significantly higher than the critical value. Upon introducing his method of linear stability, Rayleigh (1879) recognised that the dynamics of the jet had to be taken into account; in particular, he determined that for all unstable wavelengths with $\lambda > \lambda_{cr}$, the one with the fastest growth rate is selected. For inviscid jets, the analysis yields $\lambda_{opt}/R_0 = 9.01$, in close agreement with Plateau.

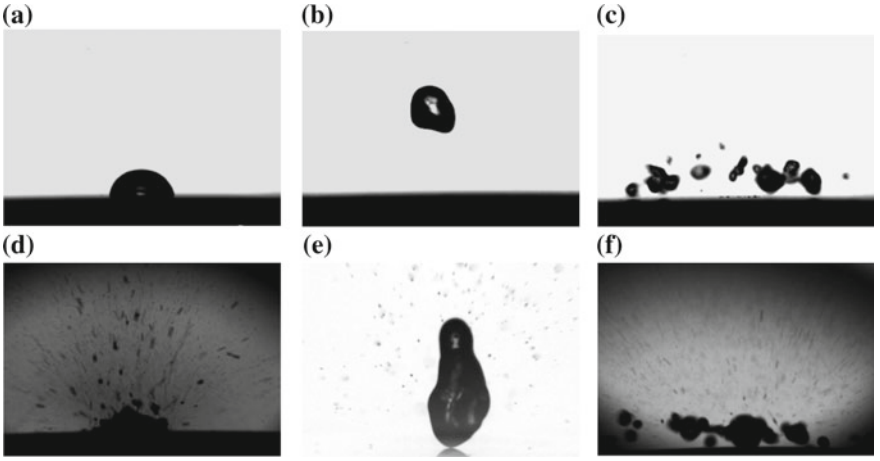

Fig. 1 Newtonian drop impact regimes on heated surfaces: **a–c** simple regimes (deposition, rebound, breakup); **d–f** mixed regimes (secondary atomisation, rebound with secondary atomisation, breakup with secondary atomisation)

According to Rayleigh's approach, an initial disturbance in a jet, α, will exhibit an exponential growth with amplitude of the form $\alpha(t) = \alpha_0 e^{-i\omega t}$, where the inviscid dispersion relation is given by

$$\omega^2 = -\frac{\sigma}{\rho R_0^3}[1 - (kR_0)^2]kR_0\frac{I_1(kR_0)}{I_0(kR_0)} \tag{5}$$

and $\omega(k)$ is the growth rate. In Eq. 5, σ is the surface tension, k is the longitudinal wave number, ρ is the fluid density and $I_n(kR_0)$ is a modified Bessel function of the first kind. The largest growth rate occurs at $kR_0 = 0.697$, which corresponds to $\lambda_{opt} = 9.01R_0$ ($k = 2\pi/\lambda$); this however does not account for viscous effects.

The effects of viscosity on capillary breakup were first investigated by Plateau (1867) and Weber (1931). Plateau found that as viscous forces become increasingly dominant with respect to inertial forces, the most unstable wavelength increases, corresponding to the greatest reduction in surface area. The growth rate is eventually determined by a balance between surface tension and viscous forces, most simply characterised by the Reynolds number. Chandrasekhar (1961) analysed the problem using the full Navier–Stokes equations, and found an implicit equation that in the limit of both small kR_0 and Re can be written as follows:

$$\omega = \omega_0([\frac{1}{2}x^2(1 - x^2) + \frac{9}{4}Re^{-2}x^4]^{\frac{1}{2}} - \frac{3}{2}Re^{-1}x^2) \tag{6}$$

where $x = kR_0$. The viscous dispersion relation for the fastest growing mode is given by

$$\omega = \frac{1}{6}\omega_\nu(1 - kR_0) \tag{7}$$

where $\omega_\nu = \sigma/R_0\rho\nu$ is the viscous growth rate and ν is the kinematic viscosity.

Close to drop pinch-off, the classical linear stability breaks down and the fluid behaviour enters a regime of self-similar flow, wherein flow lacks a typical scale and the balance of inertial, surface tension and viscous forces become independent of the minimum thickness of the neck filament attaching the falling drop to the capillary (Eggers 1997). In other words, the flow dynamics of viscous fluids in this regime can be characterised by universal scaling functions. In the last stages of detachment, viscous fluid drops can exhibit long and thin threads. After the breakdown of the linear instability, the fluid enters a regime of viscous dominated self-similar Stokes flow (Papageorgiou 1995). Temporal variations in minimum axisymmetric drop neck thickness vary as

$$D_N = \chi\frac{\sigma}{\nu\rho}(t_0 - t) \tag{8}$$

where $\chi = 0.0709$ is the universal scaling parameter determined from $\chi = 1/12(1 + \delta)$ and $\delta = 0.175$ is a positive constant to control the extent of the similarity region.

In practice, the breakup of a liquid jet generated by a plain orifice nozzle is also a function of the fluid velocity at the nozzle outlet, as shown in Fig. 2, which displays the different atomisation regimes along with the *jet stability curve*, which represents the distance from the orifice where jet breakup first occurs (Lin and Reitz 1998; Lefebvre 1988). At very low speed, the jet is essentially affected by gravity, which results in a dripping regime. As the jet speed increases, capillary forces dominate the atomisation process in a regime typically referred to as the Rayleigh breakup regime. For both dripping and Rayleigh regimes, droplet pinching occurs reasonably axisymmetrically at the centreline of the jet, producing drops that are comparable in size to the orifice diameter. At higher velocities, aerodynamic interactions with the ambient gas lead to additional instability of the surface in what is known as *wind-induced* regime. The jet breakup occurs also on the jet surface and periphery and forms drop substantially smaller than the diameter of the orifice. At higher velocities, one finds the atomisation regime, characterised by the appearance of a spray, i.e. a collection of very small drops around a liquid core that vanishes at some distance downstream of the orifice.

Whilst there is a significant volume of literature about single drop impacts and atomisation of simple (Newtonian) fluids, the number of works about fluids with complex microstructure (polymer melts or solutions, gels, pastes, foams, emulsions, etc.) is comparatively very small. However, these fluids are frequently used in common applications, such as painting, food processing and many others. Moreover, with a better understanding of the microscopic structure of complex liquids, working fluids can be tailored specifically to optimise existing industrial processes, by altering their formulation (e.g. by means of chemical additives) in such a way as to change

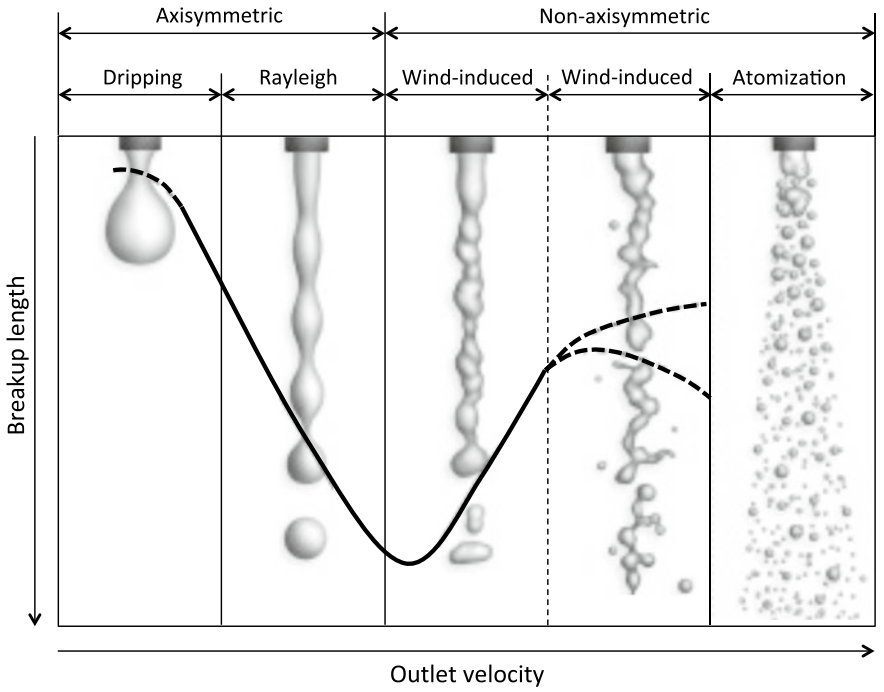

Fig. 2 Atomisation regimes arising from a plain orifice nozzle. Adapted from Bonhoeffer et al. (2017)

one or more physical properties. In the following, the main results about drop impact and atomisation of non-Newtonian fluids are reviewed.

2 Impact of Viscoelastic Drops on Solid Surfaces

2.1 Impact on Homothermal Surfaces

The impact dynamics of viscoelastic drops on solid surfaces did not receive significant attention until about 20 years ago, when high molecular weight flexible polymers were introduced to improve agrochemical formulations (Bergeron et al. 1998, 2003). It was found that very small amounts (of the order of 100 ppm) of high molecular weight flexible polymers, such as polyethylene oxide (PEO), can reduce the tendency of drops to rebound after impacting on low surface energy (hydrophobic) surfaces, which can be exploited to control many spray applications and, in particular, the distribution of agrochemicals (Williams et al. 2008).

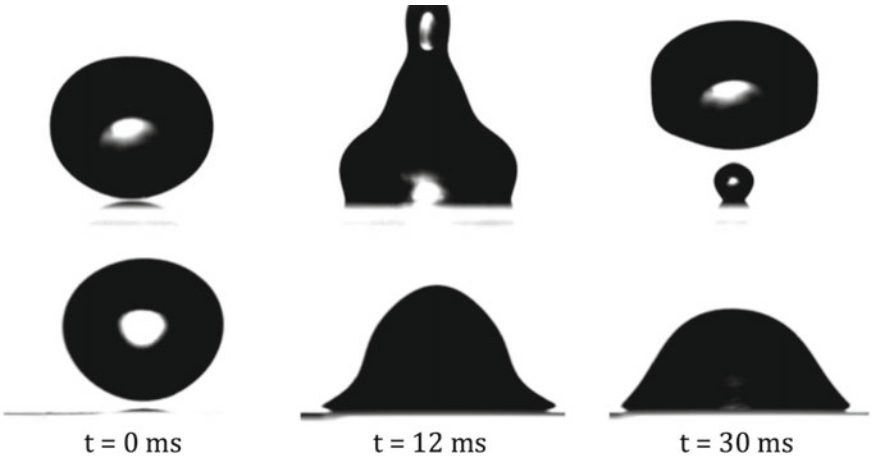

Fig. 3 Impact of water (top) and 200 ppm polymer solution (bottom) drops ($D_0 \approx 3$ mm) impacting on a PTFE surface (release height: 20 mm)

This phenomenon is illustrated in Fig. 3, which compares the impact morphologies of two drops, one of de-ionised water and one of a 200 ppm PEO solution in the same water, impacting with the same velocity on a PTFE surface (equilibrium contact angle with water: ≈110°). After the initial inertial spreading, which is similar for both drops, water drops exhibit fast recoil (≈30 ms) under the action of surface forces, which evolves into almost complete dewetting, and rebounds on the impact surface. On the contrary, the recoil of polymer solution drops is very slow and terminates in a sessile equilibrium state only after several seconds. This is somewhat counter-intuitive because the shear viscosity and surface tension of such drops are almost identical to those of pure water (Crooks et al. 2001).

Indeed, it took several years to develop a correct understanding of this phenomenon. Initially, the effect of polymer additives on drop rebound was interpreted in terms of the bulk rheology of the fluid, namely, the fluid elongational viscosity, which was thought to provide a large resistance to drop retraction after impact, thereby suppressing droplet rebound (Bergeron et al. 2000; Crooks et al. 2001). However, this interpretation has an obvious weakness, because the large velocity gradients to achieve significant magnitudes of elongational viscosity are observed during the inertial expansion, which has a timescale of ≈5 ms, while their effect on drop retraction spans over several seconds. In addition, if energy dissipation occurs during inertial spreading, both the spreading velocity and the maximum spreading diameter of polymer solution drops should be smaller than those of water drops, whereas experimental data suggest there is little or no difference. Later on, it was demonstrated that some of the elongational viscosity data used to support this interpretation of the phenomenon exhibit very poor reproducibility as the same researchers attempted to repeat measurements on the same polymer solutions (Bertola 2013), as shown in Fig. 4.

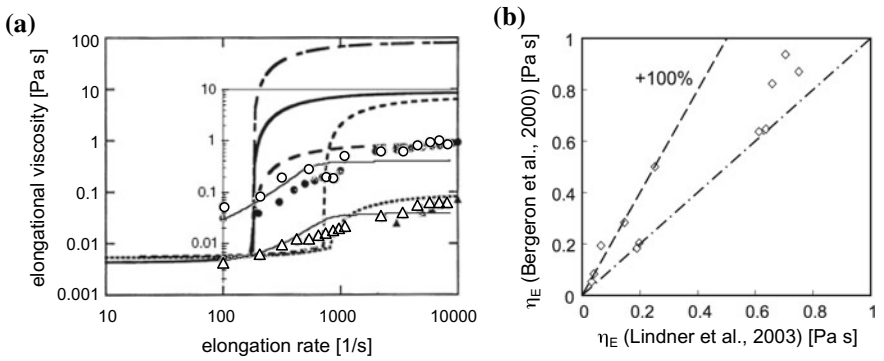

Fig. 4 Elongational viscosity versus elongation rate measurements made with a Rheometrics RFX opposing nozzle for two dilute PEO polymer solutions: 0.25 g/l, molecular weight 4×10^6 (circles); 1.0 g/l, molecular weight 2×10^6 (triangles). **a** Comparison between data by Bergeron et al. (2000), open symbols, and Lindner et al. (2003), filled symbols. **b** A direct comparison in linear scale shows data by Bergeron et al. (2000) are sometimes identical, sometimes up to twice as large as those by Lindner et al. (2003)

More recently, it was suggested that the contact line dynamics is ruled by the competition between the surface tension that drives the retraction and the elastic normal stresses that counter it (Bartolo et al. 2007). In particular, using a generalised lubrication equation accounting for capillarity and normal stresses in addition to shear stresses, it was found that the retraction velocity, v_r, is related to the first normal stress coefficient, Ψ, as $v_r \sim 1/\Psi^{-1/2}$. The main argument against this approach is that dilute polymer solutions do not exhibit appreciable normal stresses in the range of shear rates observed in impacting drops during the retraction stage (Lindner et al. 2003; Bartolo et al. 2007), and therefore the proposed theory cannot explain the slowing down of recoil observed in dilute polymer solution drops. Unfortunately, the theory was naïvely (or perhaps cleverly) validated with experimental data relative to solutions with a content of polymer well above the overlap concentration, i.e. in the semi-dilute regime, and still receives much credit to date, see e.g. Chen et al. (2018) or Wang et al. (2017). Other flaws and mistakes of this work are discussed in detail by Bertola (2013).

Several independent experiments provide evidence that the slowing down of drop retraction is not related to the bulk rheological behaviour of the fluid. A study of drops impacting on small targets, which remove the influence of the substrate, demonstrated that polymer additives do not change the retraction velocity in comparison with water drops (Rozhkov et al. 2003). This suggests that the polymeric additives do not have any effect on the bulk elongational deformations of the drop but instead they influence the interaction of the lamella with the substrate at the retraction stage when the impact happens on a plane, smooth and solid substrate.

Another way to completely remove the influence of the substrate is heating the impact surface to create a thin vapour film between the drop and the substrate, which is known as *dynamic Leidenfrost phenomenon* (Rein 2003; Quéré 2013). Experiments

on Leidenfrost drops of dilute polymer solutions showed that polymer additives cause only a slight reduction of the maximum spreading diameter and of the retraction velocity with respect to water drops (Bertola 2009b, 2014; Black and Bertola 2013), which is by no means comparable with the large reduction of the retraction velocity observed during the impact on solid surfaces. Because in these experiments wetting effects are absent or negligible, one must conclude that the retraction velocity reduction observed in drops containing flexible polymers impacting on solid surfaces is due to the drop–surface interaction rather than to an increased energy dissipation connected to the elongational viscosity of the fluid. In addition, the maximum bouncing height of viscoelastic drops can be significantly higher than that of Newtonian drops; since this quantity represents the fraction of the initial kinetic energy which is not dissipated during impact, these experiments suggest that in some cases polymer additives indeed reduce instead of increasing the overall energy dissipation. A more detailed analysis of viscoelastic Leidenfrost drops is discussed in Sect. 2.2.

These results indicate that the impact dynamics of viscoelastic drops impacting on solid surfaces is mainly driven by wetting rather than by the bulk rheology of the fluid such as the elongational viscosity or the normal stress coefficient. A deeper understanding of the underlying physical mechanism can be obtained through the analysis of four apparently independent aspects (Smith and Bertola 2010b): (i) the velocity field inside the impacting drop; (ii) the apparent dynamic contact angle; (iii) the microscopic contact line morphology and (iv) the polymer conformation near the receding contact line.

Fluid velocity inside impacting droplets The simplest way to quantify the effects of bulk viscous dissipation on fluid flows is to measure velocities and velocity gradients; in the case of impacting droplets, these measurements are not simple because of the small length- and timescales of the process. Recent particle velocimetry measurements inside impacting drops showed that the local velocities measured during expansion and retraction are similar for the drops of polymer solution and for those of pure water (Smith and Bertola 2010a, 2011). Drops were seeded with fluorescent colloids (2 μm diameter), with a concentration of approximately 0.001 wt.%. Movies for particle velocimetry were collected at 2000 fps and, using stroboscopic illumination at a frequency of 8 kHz, each particle was captured four times along its radial trajectory in a single frame. The particles trajectories were then extrapolated to estimate the position of the drop centre and correspondingly the radial distance of each particle, within a negligible error. The velocity at each radial position (i.e. the Eulerian velocity field) was calculated as the distance between two images of the same particle divided by the time interval between two pulses of the stroboscopic illumination.

Figure 5 compares the local, instantaneous velocities measured in a water drop and in a 200 ppm polyethylene oxide solution drop, showing that the velocity fields in the two drops are similar both qualitatively and quantitatively during the inertial expansion as well as during the drop retraction. The velocity gradient in the fluid, obtained from the slope of radial velocity profiles, gives an indication of the rate of deformation of fluid elements within the drop, hence the effects of the elongational

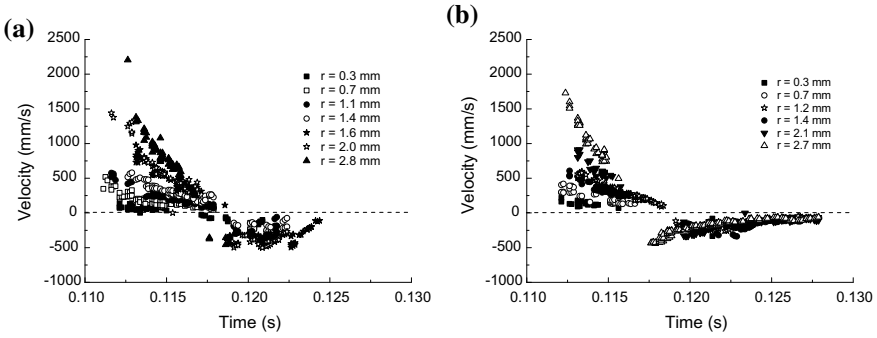

Fig. 5 Fluid velocity measured inside impacting drops at different radial positions during inertial spreading and retraction; **a** water; **b** 200 ppm polyethylene oxide (molecular weight: 4,000 kDa) solution. The impact velocity is about 1.4 m/s, and the plane of focus is set at a distance of about 10 μm above the impact surface

viscosity. Figure 6a shows that the velocity gradients measured in the water and polymer solution drops during the inertial spreading are almost identical; although the magnitude of these velocity gradients is of the order of 10^2 s^{-1}, it is not sufficient to induce polymer molecules' stretching, which require velocity gradients of the order of 10^2 s^{-1} and above (Crooks et al. 2001). During retraction, radial velocity gradients are significantly smaller than those observed during inertial spreading, and fluid elements are in compression rather than extension, which makes the stretching of molecules inside the drop very unlikely (de Gennes 1974).

Whilst velocities and velocity gradients measured inside the droplet are almost identical for water and dilute polymer solutions, a comparison of the fluid velocity in the bulk of the droplet during retraction with the velocity extracted from macroscopic observations of the contact line (i.e. the rate of change of the drop base diameter) shows a dramatic difference between water and PEO drops. Figure 6b shows that the velocity of the contact line for droplets of pure water at the onset of retraction is similar to that of the bulk fluid. By contrast, the motion of the contact line for PEO drops is one order of magnitude slower than that of the corresponding bulk velocity measurements, and further confirms that the difference between the behaviours of the two fluids occurs only at the droplet edge.

Dynamic contact angle The apparent contact angle is perhaps the most significant quantity used to characterise the wetting behaviour of liquids on solid surfaces and the dynamics of drop recoil following inertial spreading. Surprisingly, all of the early attempts to explain the phenomenology of dilute polymer solution drop impact completely ignore dynamic contact angle measurements (Bergeron et al. 2000; Crooks et al. 2001; Bartolo et al. 2007).

A qualitative picture of the contact angle dynamics of water drops and polymer solution drops impacting on the same surface with the same impact Weber number can be obtained from the side views displayed in Fig. 3, which suggest that the polymer additive significantly reduces the dynamic contact angle with respect to pure water;

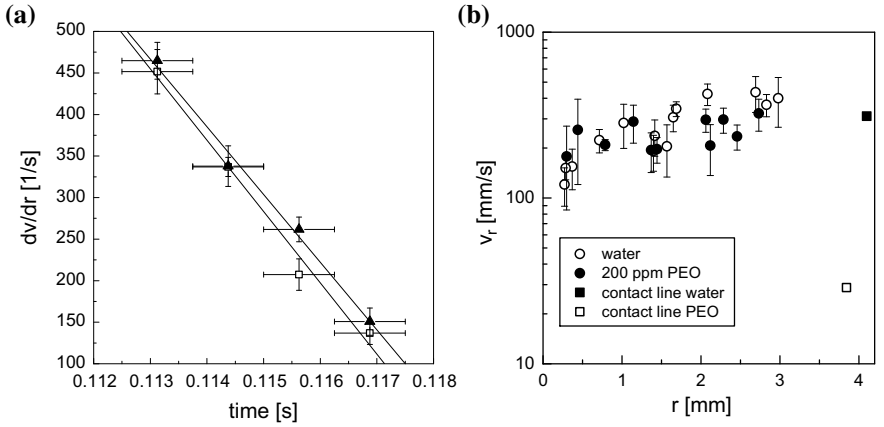

Fig. 6 Velocity gradients measured inside impacting drops during inertial spreading (**a**); comparison between the fluid velocities measured at the largest radial position ($r/R_0 \approx 3.5$) and the contact line velocities of a water drop and a 200 ppm polyethylene oxide (molecular weight: 4,000 kDa) solution drop (**b**). Adapted from Smith and Bertola (2011)

however, the change is localised in the wedge near the contact line, as if the contact line was pinned on the surface, while the bulk fluid seems to flow back towards the drop centre without encountering the same resistance.

Systematic comparative measurements of the apparent dynamic contact angle during drop impact (Bertola 2010; Bertola and Wang 2015) demonstrated that while no differences can be observed between water drops and polymer solution drops during inertial spreading, there are significant differences during the retraction stage. The typical behaviours of the base diameter and of the dynamic contact angle obtained from digital image processing (Biolè and Bertola 2015a, b; Biolè et al. 2016) are displayed in Fig. 7, for two drops impacting on a PTFE surface at low Weber number ($We \approx 15$). The base diameter of water drops (Fig. 7a) grows and decreases approximately at the same rate, and becomes equal to zero at the moment of drop rebound, about 50 ms after impact. After rebound, it reaches the final equilibrium value after a few oscillations, typically in a very short time (20–30 ms). With the exception of a discontinuity in correspondence of the drop rebound, the apparent contact angle has an oscillatory behaviour around the equilibrium value and its magnitude remains bounded between the values of the advancing and receding contact angles.

In polymer solution drops, both the base diameter and the dynamic contact angle are significantly different, as shown in Fig. 7b. The base diameter initially grows at the same rate as in water drops and reaches a maximum approximately of the same magnitude; however, the retraction phase is much slower, and the base diameter takes several seconds to reach the equilibrium value. The retraction phase is characterised by stick-slip dynamics of the drop edge, which corresponds to rapid fluctuations of the base diameter in phase with the dynamic contact angle minima. Unlike in the case of water drops, the dynamic contact angle initially decreases significantly as the drop

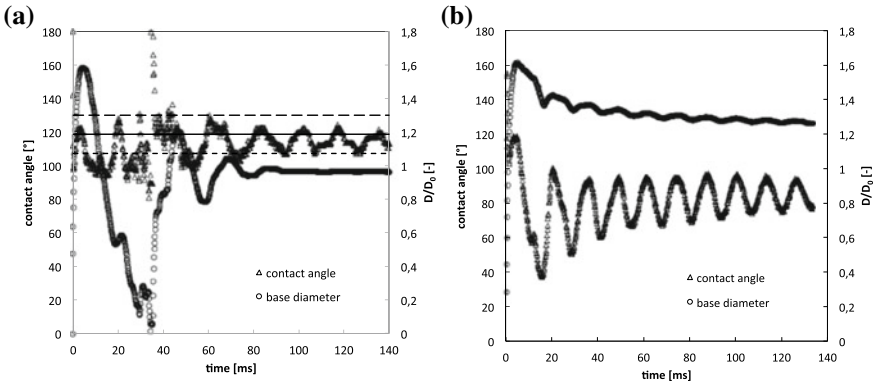

Fig. 7 Base diameter and dynamic contact angle of **a** a water drop and **b** a 200 ppm polyethylene oxide solution drop, impacting on a PTFE surface with $We \approx 15$. The horizontal solid line corresponds to the equilibrium contact angle ($\theta_e = 119°$), while the long- and short-dashed lines correspond to the advancing ($\theta_a = 130°$) and receding ($\theta_r = 107°$) contact angles, respectively

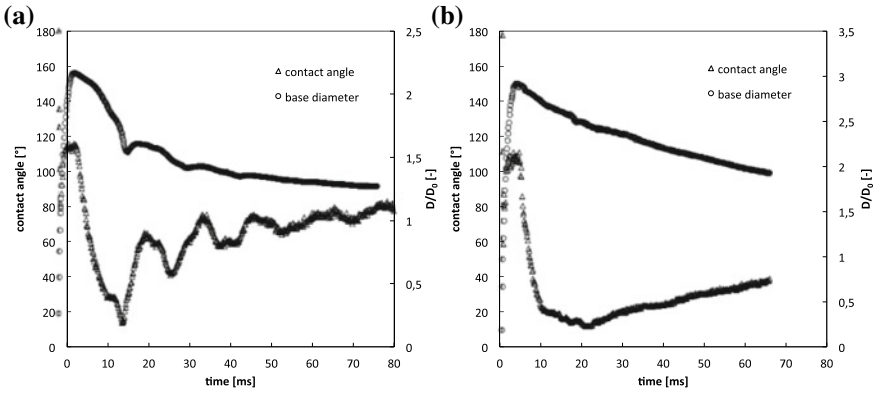

Fig. 8 Base diameter and dynamic contact angle of a 200 ppm polyethylene oxide solution drop impacting on a PTFE surface with **a** $We \approx 55$ and **b** $We \approx 110$

retracts, and then slowly returns to the equilibrium value in an oscillatory fashion. The local minima of these oscillations correspond to the stick-slip fluctuations of the base diameter. During the approach to the equilibrium value, the dynamic contact angle of dilute polymer solution drops remains smaller than the contact angle measured with water drops under the same experimental conditions.

For increasing impact Weber numbers (Fig. 8), the contact line stick-slip is limited to the first contact angle oscillation, and the recoil velocity becomes increasingly smaller. The initial decrease of the dynamic contact angle can attain very small values ($\lesssim 20°$), while the contact angle oscillations gradually die out as the impact Weber number increases.

A simple interpretation of this behaviour can be given in terms of the Young–Laplace force balance: a small contact angle corresponds to a large horizontal component of the liquid–vapour interfacial force that drives the drop retraction. Thus, since the contact angles observed during the retraction of polymer solution drops are significantly smaller than those observed in drops of pure water, one can conclude that the receding movement of the contact line of polymer solution drops requires a larger driving force than in the case of water. It must be remarked that, strictly speaking, the Young–Laplace equation should not be applicable even if the radial velocity is zero because the system is out of equilibrium; however, this approach is still justified because the timescale of the phenomenon is still much longer than molecular timescales ($\sim 10^7 \div 10^9$ s) (Barnes et al. 1995; Borodin and Smith 2000).

Because the advancing contact angle (during drop spreading) is similar for all drops, one can also conclude that polymer solution drops show larger contact angle hysteresis. Contact angle hysteresis around the equilibrium value is generally understood in terms of roughness and/or chemical heterogeneity of the surface (de Gennes 1985). However, more recently, it has been proposed that the contact angle hysteresis may be caused by a liquid film left behind the contact line during retraction (Chibowski 2003, 2007). Since both drops of pure water and those of polymer solution impact on identical surfaces, the difference observed in the contact angle hysteresis cannot be interpreted in terms of surface roughness or chemical heterogeneity. Thus, it can be argued that the polymer additive changes either the chemical structure of the surface, or the properties of the liquid film left behind the contact line during retraction, or both.

The advancing or receding contact line of a liquid drop moving on a solid surface is often described by introducing the concept of line tension (Tadmor 2011):

$$\Pi = \sigma \frac{D}{2}(cos\theta - cos\theta_{eq}) \tag{9}$$

where D is the drop base diameter, and θ_{eq} and θ are the equilibrium and the apparent contact angles, respectively; this approach is equivalent to Furmidge's equation (Dussan 1985). When the radial force per unit length due to polymer stretching, F_P, is taken into account, Eq. (9) becomes

$$\Pi + F_P \frac{D}{2} = \sigma_P \frac{D}{2}(cos\theta_P - cos\theta_{eq,P}) \tag{10}$$

where σ_P is the surface tension of the polymer solution, and $\theta_{eq,P}$ and θ_P are the equilibrium and the apparent contact angles of the polymer solution drop, respectively; since $\sigma_P \approx \sigma$ and $\theta_{eq,P} \approx \theta_{eq}$, one finds

$$F_P/\sigma \approx (cos\theta_P - cos\theta) \tag{11}$$

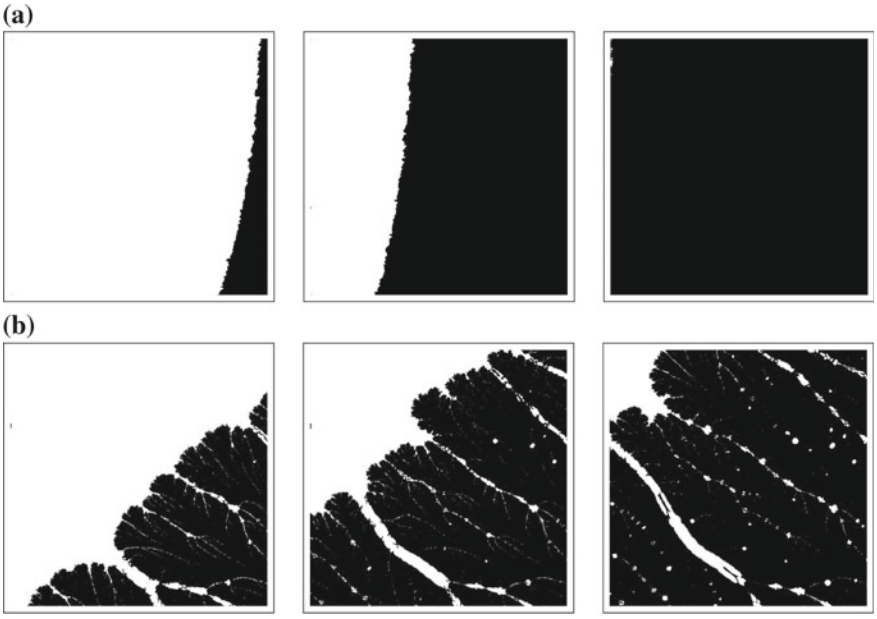

Fig. 9 Microscopic contact line morphology during drop retraction after impact on a hydrophobised glass substrate with Weber number $We \approx 110$: **a** pure water; **b** 200 ppm polyethylene oxide solution. Images are enhanced by background subtraction, histogram equalisation and conversion to binary. Each frame has a size of 700 μm

Using Eq. (11), one can estimate the additional contact line tension arising in dilute polymer solutions from dynamic contact angles of water and polymer solution drops.

Contact line morphology An example of the microscopic contact line morphology during drop retraction on a hydrophobised glass substrate is displayed in Fig. 9, which compares the contact lines of drops of pure water and of a dilute polymer solution in the same experimental conditions. While the contact line of the water drop appears almost perfectly smooth, the contact line of the polymer solution drop exhibits large local deformations, and leaves behind microscopic liquid filaments as it sweeps the surface. Filaments are distributed uniformly around the contact line and their width ranges between approximately 2 μm and 30 μm. The structure and density of these filaments depend on the polymer concentration in the fluid: for $c < 100$ ppm, one can observe linear filaments oriented in the radial direction and their density being increased with the polymer concentration; for $c \gtrsim 100$ ppm, there are less but thicker filaments, displaying numerous dendritic ramifications.

Filaments evolve following a capillary instability mechanism, until they locally break up into secondary microscopic droplets, in a similar fashion to the well-known beads-on-a-string breakup mechanism characteristic of many viscoelastic

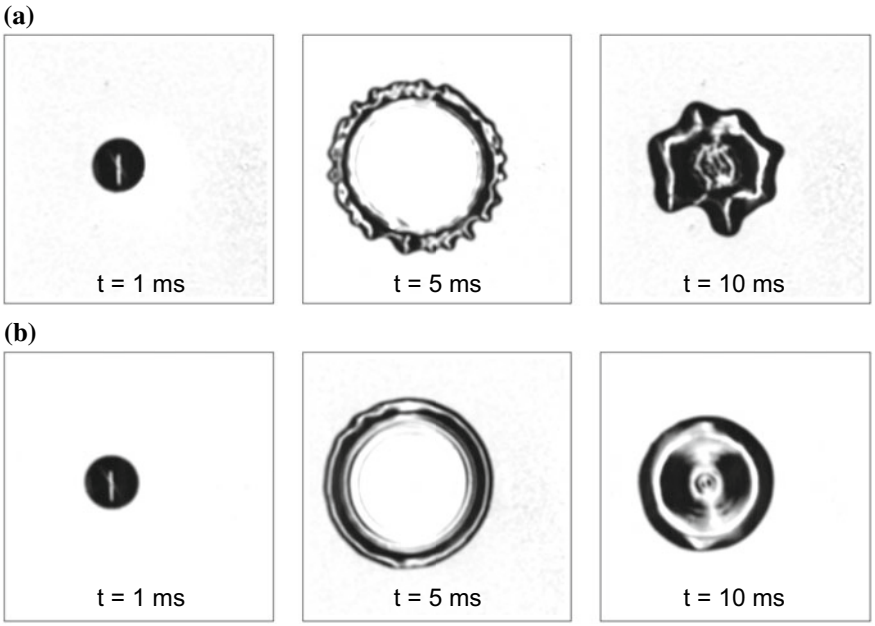

Fig. 10 Contact line morphology during drop impact on a hydrophobised glass substrate with Weber number $We \approx 110$: **a** pure water; **b** 200 ppm polyethylene oxide solution

fluids (Oliveira et al. 2006). At higher polymer concentrations, filaments are more stable, and therefore the breakup mechanism is less noticeable on the timescale of the experiment.

This complex morphology, which can be observed only at the microscale, suggests that even from the macroscopic point of view, the term *contact line* is not appropriate to indicate the drop edge, but one should rather use the expression *apparent contact line*, similar to the convention used for contact angles. Figure 9 also demonstrates the importance of image processing in the identification of the thinner filaments and the smaller beads, which could hardly be observed in raw images.

If the contact line is observed from a macroscopic point of view, the microscopic contact line features peculiar of dilute polymer solution drops are no longer visible. On the contrary, the contact line of polymer solution drops appears smoother than the contact line of water drops, as shown in Fig. 10.

The microscale analysis of the contact line morphology provides a key to understanding the peculiar behaviour of polymer solution drops as compared with water drops. In particular, the liquid filaments left behind by the receding contact line suggest that the conformational change of polymer coils, which originates viscoelastic behaviour is localised near the contact line, while in the rest of the droplet non-Newtonian effects are negligible. In this framework, the reaction force of the stretched polymer coils on the contact line represents an additional contribution to the line

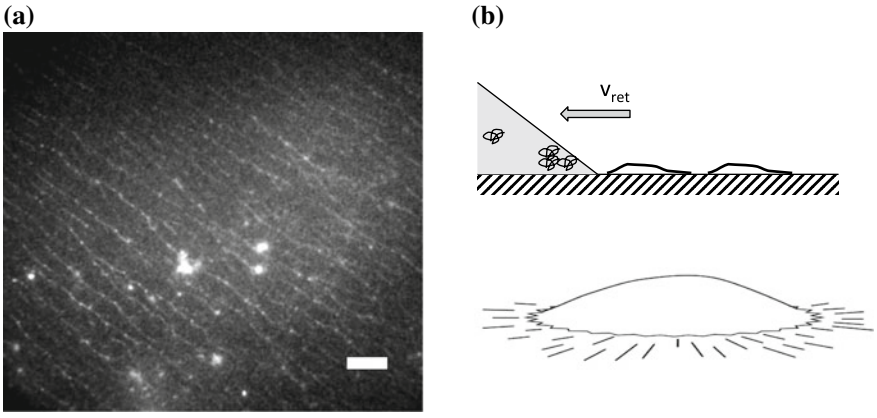

Fig. 11 Polymer conformation observed on the substrate behind the receding contact line of a dilute polymer solution drop containing fluorescent λ-DNA. **a** Image of stretched λ-DNA molecules collected at a frame rate of 1000 fps with an exposure time of 400 μs; the white reference bar corresponds to the length of a fully stretched DNA molecule. **b** Pictorial description of the polymer dynamics during drop retraction: as the meniscus recedes, polymer molecules in the liquid wedge are stretched by molecular combing. Copyright (2010) by The American Physical Society

tension, which causes the reduction of the apparent dynamic contact angle during drop recoil, as discussed above.

Polymer conformation near the contact line The nature of the dissipative phenomena arising near the contact line during drop retraction was revealed by visualisation experiments aiming at the direct observation of the polymer conformation as well as the contact line morphology at the microscopic scale (Smith and Bertola 2010a; Bertola 2013; Biolè and Bertola 2015c).

To investigate the dynamics of polymer molecules during drop retraction, and its potential effect on the velocity of the receding contact line, fluorescent λ-DNA (a linear biopolymer with a random coil conformation, a diameter of about 1.4 μm, a stretched length of about 22 μm, and thus visible using a fluorescent microscope) was added to the impacting drop and observed through an optical microscope equipped with image intensifier (Smith and Bertola 2010a, b). After the passing of the contact line, stretched DNA molecules can be observed on the substrate, oriented in the direction perpendicular to the contact line, as shown in Fig. 11a. Independent experiments on forced dewetting showed that polymer deposited on the substrate results in a velocity-dependent force at the contact line (Smith and Sharp 2014). This bears strong similarities with other DNA stretching methods, such as molecular combing or air blowing techniques (Kim et al. 2007); in these techniques, DNA molecules are stretched using combination of hydrodynamic and surface forces arising when a liquid meniscus moves on a solid surface. For example, in molecular combing such meniscus is created by slowly pulling out a plate from a solution containing DNA. The same conditions occur when an impacting droplet retracts on the target surface

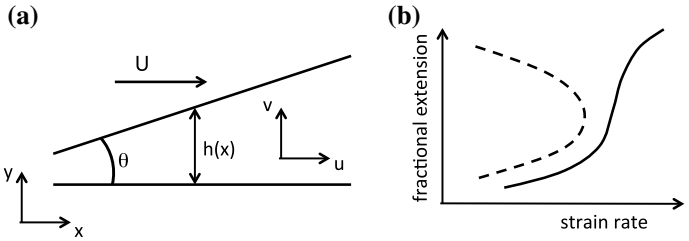

Fig. 12 Schematic of the liquid wedge near the contact line (**a**) and schematic of supercritical coil–stretch transition (de Gennes 1974) (**b**)

after maximum spreading, the only difference being that this process is orders of magnitude faster than molecular combing, where the typical velocity of the meniscus is 0.2 mm/s. This mechanism is illustrated qualitatively in Fig. 11b, and can be easily modelled as a supercritical coil–stretch transition induced by the shear flow in the liquid wedge near the contact line (de Gennes 1974).

The hydrodynamics of the liquid wedge near the contact line can be modelled as the flow between a fixed horizontal surface (the substrate) and a plate inclined at an angle θ (corresponding to the instantaneous value of the apparent dynamic contact angle), moving at velocity U, as shown schematically in Fig. 12a. The minimum thickness of the liquid film, h_0, must be no less than the unperturbed size of the polymer coils, R_0; for polyethylene oxide molecules in water, one finds $R_0 = 0.0888M^{0.5} = 178$ nm, where M is the molecular weight (Brandrup et al. 2005), and hence one can take an order of magnitude $h_0 \approx 0.2$ μm. Polymer coils are subject to hydrodynamic interaction with the solvent, with a characteristic Zimm time $\tau_0 \approx 0.2\eta_s R_0^3/k_B T = 0.27$ ms and a Rouse time $\tau_R \approx 2R_h\eta_s R_0^2/\pi k_B T = 0.41$ ms, where η_s is the solvent viscosity.

At this point, it is important to note that the magnitude of U, i.e. the main parameter of the process, is not necessarily equal to the contact line velocity during drop retraction. Previous works (Bertola 2013; Smith and Bertola 2010a, 2011) show that while in water drops the fluid velocity is the same as the velocity of the receding contact line, in dilute polymer solution drops, the contact line velocity is two or three orders of magnitude smaller than the bulk velocity of the fluid during retraction.

In a reference frame originating on the contact point, the velocity components parallel and perpendicular to the substrate during drop retraction are, respectively, $u \approx Uy/h(x)$ and $v \approx \xi(\theta)x$, where $h(x) \approx \theta x$ is the liquid film thickness and $\xi(\theta)$ is a positive function of the apparent contact angle (see Fig. 12a). The velocity gradient of this flow field can be split into its symmetrical part, $A = \frac{1}{2}(u_y + v_x) = \frac{1}{2}(U/h + \xi)$, associated with a pure deformation, and its anti-symmetrical part $\omega = \frac{1}{2}(u_y - v_x) = \frac{1}{2}(U/h - \xi)$, associated with a pure rotation. Since $\xi(\theta) > 0$, $\omega/A < 1$, therefore it is possible to have strong distortions of the polymer coils, even in the absence of elongational flow (Lumley 1973). This corresponds to a second-order transition from coil to stretch conformation state, i.e. with a constantly positive slope

of the stretching ratio, $l = r/L$, where r is the polymer elongation and L is the length of the fully stretched chain, with respect to the order parameter $\xi(\theta)$ (i.e. $dl/d\xi > 0$), as illustrated schematically in Fig. 12b (de Gennes 1974).

Following the classical finite extensibility approach Peterlin (1966), the stretching ratio is related to the velocity gradient as

$$l = \frac{3}{Z\mathcal{L}^{-1}(l)} \left\{ 1 + \frac{1}{6} \frac{\left(\frac{U}{h} + \xi\right)^2 \tau^2}{\frac{9l^2}{\left[\mathcal{L}^{-1}(l)\right]^2} - \frac{U}{h}\xi\tau^2} \right\} \tag{12}$$

where τ is the relaxation time, which is given by de Gennes (1974)

$$\tau(l) \approx \frac{\tau_R}{1 + \frac{1}{l}} \tag{13}$$

and $\mathcal{L}^{-1}(l)$ is the inverse Langevin function, which can be estimated, for example, using Kroger's approximation Kroger (2015):

$$\mathcal{L}^{-1}(l) = \frac{3l - (l/5)(6l^2 + l^4 - 2l^6)}{1 - l^2} \tag{14}$$

The resulting recall force of a stretched polymer coil is

$$F = \frac{k_B T L}{R_0^2} \mathcal{L}^{-1}(l) \tag{15}$$

The ensemble of polymer molecules stretching as the drop edge sweeps the surface provides the dissipative force necessary to slow down the displacement of the contact line. This can be interpreted, from a macroscopic point of view, as an additional, dissipative force acting on the contact line and opposed to its movement, or an effective contact line friction. This also explains the reduction of the dynamic contact angle observed in experiments: to overcome the action of polymer molecules on the contact line, the horizontal component of the surface force driving the droplet retraction must be larger than in a Newtonian fluid, and therefore the apparent dynamic contact angle must be smaller.

2.2 *Impact on Heated Surfaces*

Early studies about the impact of viscoelastic drops on heated surfaces focused primarily on dilute polymer solution drops and found significant differences with respect to the impact morphology of Newtonian drops (Bertola 2004); in particular, it was observed that adding small amounts of a flexible polymer to the aqueous phase, secondary atomisation can be suppressed completely (Bertola and Sefiane 2005), and

droplet rebound in the Leidenfrost regime, i.e. when a stable vapour film separates the drop from the impact surface, is significantly enhanced (Bertola 2009b). More recently, it was shown that Leidenfrost rebounds are only weakly affected by the polymer concentration (i.e. by the fluid rheology) (Bertola 2014), but can be related to the symmetry of the rebound process (Chen and Bertola 2016b).

Since the fluid properties (surface tension, viscosity and relaxation time), and consequently the dimensionless parameters, are strongly dependent on temperature, it is necessary to estimate the drop temperature accurately. In particular, the drop temperature depends on nature of the liquid–surface interface and on the contact duration. If the liquid wets the surface for a sufficiently long time, it can reach the boiling point, after which temperature remains constant; vice versa, if the contact time is very short and the liquid does not wet the surface, the drop heating can be negligible.

Suppression of secondary atomisation and splashing The most evident effect of the fluid viscoelasticity on the morphology of drops impacting on heated surfaces is perhaps the suppression of secondary atomisation and the significant limitation of the range of experimental conditions where drop breakup occurs (Bertola 2004). Figure 13 shows an example of comparison between the impact morphology of a water drop and a dilute polymer solution (200 ppm PEO in water) drop having the same diameter and impacting with the same Weber number on a surface kept at constant temperature; while the water drop exhibits breakup with secondary atomisation upon impact, the polymer solution drops exhibit only a small rebound without any liquid mass loss.

In Newtonian drops, secondary atomisation can also be observed during drop rebound (see Sect. 1); for a given value of the impact Weber number, dry rebound (i.e. without secondary atomisation) occurs only above a certain temperature, which is often referred to as *dynamic Leidenfrost temperature* (Wang et al. 2000); its value has been shown to increase with the Weber number (Yao and Cai 1988).

It should be observed that both the inhibition of drop breakup and the suppression of secondary atomisation cannot be explained only with the increase of the Ohnesorge number, because the shear viscosity of these polymer solutions is only 20–50% higher than the viscosity of the solvent. Thus, their origin must be related at least partially to the fluid elasticity. In particular, one can identify three independent mechanisms that affect either drop breakup or secondary atomisation, or both. First, the elongational viscosity is known to change substantially the breakup dynamics of free-surface flows and their decay into drops (Bazilevskii et al. 1981; Rozhkov 1983); thus, elongational viscosity opposes the scattering of secondary droplets from the free surface of the impacting drop, as well as the detachment of satellite drops from the rim during corona splashing. Second, polymer additives improve the stability of the surface between the drop and the surrounding atmosphere and, in case of Leidenfrost drops, also the surface in contact with the vapour cushion that separates the drop from the hot wall; this reduces the chances that the liquid may locally touch the wall and start boiling. Third, even in cases when the liquid makes contact with the wall with consequent bubble nucleation, the presence of the polymer can significantly affect

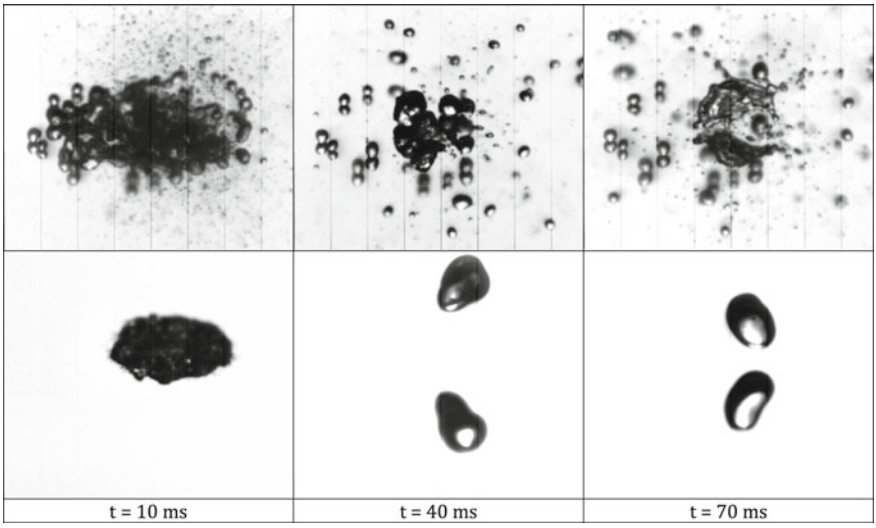

Fig. 13 Comparison between the impacts of a water drop (top) and PEO solution (concentration: 200 ppm; molecular weight: 4 MDa) drop (bottom) impacting on a polished copper surface at T = 160 °C and We = 220

the process of growth, detachment and rise of vapour bubbles (Hartnett and Hu 1986; Kim et al. 2004), and hence prevent their bursting on the drop free surface.

If one accepts the current definition of dynamic Leidenfrost temperature (the minimum temperature to observe dry rebound without secondary atomisation), one must conclude the dynamic Leidenfrost temperature of viscoelastic drops is significantly lower than that of Newtonian drops of similar viscosity.

Figure 14 compares the dynamic Leidenfrost temperatures, determined by experimental observation (Bertola and Sefiane 2005), of a water and a polymer solution drops with $D_0 \approx 3.8$ mm impacting on a polished aluminium surface. The dynamic Leidenfrost temperature of the polymer solution drop is significantly lower than that of the water drop, and is a weakly growing function of the impact Weber number; in addition, extrapolating experimental data to the limit $We \rightarrow 0$ one finds the conventional value of Leidenfrost temperature for sessile water drops on polished aluminium (Bernardin and Mudawar 2002).

As a conclusive remark, it should be observed that in the case of viscoelastic fluids, the definition of a dynamic Leidenfrost temperature is less significant than in case of simple liquids. In fact, for drops of pure water, secondary atomisation actually disappears when a continuous and stable vapour cushion prevents the drop from making contact with the hot surface, which is indeed analogous to the Leidenfrost phenomenon in sessile drops. This is no longer true when polymer additives are dissolved into the impacting drop: in fact, even if the film is unstable and the liquid locally touches the hot wall, there are other physical mechanisms that prevent scattering of satellite droplets from the free surface of the liquid, as discussed above.

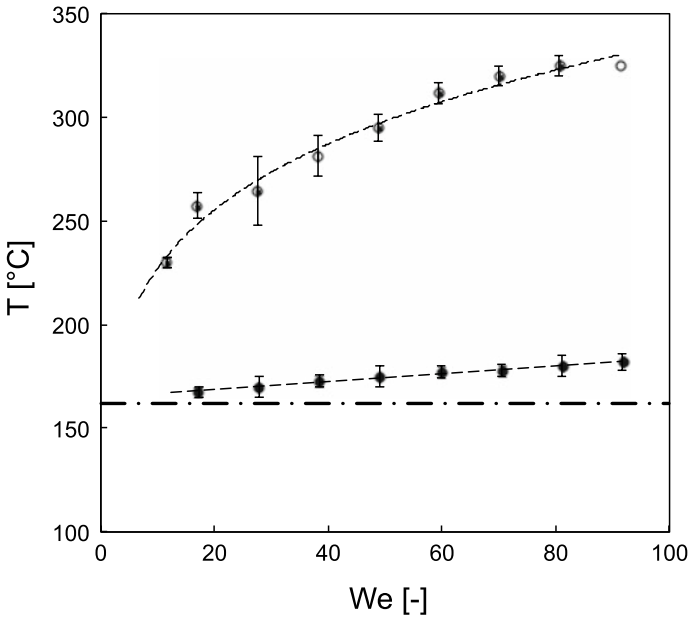

Fig. 14 Dynamic Leidenfrost temperature of water (open symbols) and 200 ppm polyethylene oxide solution (filled symbols) drops with $D_0 \approx 3.8$ mm impacting on a polished aluminium surface. The horizontal dash-dot line indicates the Leidenfrost temperature of sessile water drops on polished aluminium ($T_{L0} = 162\,^{\circ}\mathrm{C}$)

In this case, the expression 'dynamic Leidenfrost temperature' may be misleading, because it suggests the impacting drop never wets the surface, whereas wetting might occur without the development of secondary atomisation.

Viscoelastic Leidenfrost drops Above the dynamic Leidenfrost point, the vapour film between the drop and the hot surface is stable, and therefore the liquid is not in contact with the wall; thus, one can neglect the effects of wetting and wall friction (Bertola 2009b, 2014; Black and Bertola 2013). A rough estimate of the average temperature of the drop can be obtained from a lumped capacitance energy balance; neglecting the heat exchange between the liquid drop and the surrounding plume of hot air, i.e. considering only the conduction heat flux from the surface to the liquid through the liquid film, the energy balance equation can be written as

$$mC\,dT = \frac{\pi D^2 k_v}{4\delta}(T_S - T)dt \tag{16}$$

where m is the drop mass, C is the specific heat of water, D is the diameter of the drop bottom, δ is the thickness of the vapour layer, k_v its thermal conductivity, T_S is the surface temperature and T the average temperature of the drop. Integration of Eq. (16) allows one to estimate the time required for the drop to reach a certain average

temperature. The most favourable heating conditions occur when the heated surface is largest (i.e. the drop is at maximum spreading, where $D \approx 3D_0$) and the vapour film thickness is minimum ($\delta_{\min} \approx 10\mu$m) (Rein 2003); under these assumptions, the time necessary to heat a drop up to a certain temperature T is

$$t_{\min} = \frac{2\rho D_0 C \delta_{\min}}{27 k_v} ln \frac{T_S - T_{amb}}{T_S - T} \tag{17}$$

According to Eq. (17), a 3 mm diameter water drop would reach the saturation temperature in 87 ms, which is a significantly longer time than the maximum duration of the contact observed experimentally, which is around 20 ms (Bertola 2009b). If Eq. (16) is solved with respect to temperature, one can also estimate the average drop temperature after a certain time; in particular, after 20 ms, the temperature increase of a 3 mm drop is only 10 °C. Thus, one can use the fluid properties calculated at ambient temperature without introducing significant errors.

The main macroscopic quantities that characterise the impact of Leidenfrost drops are the maximum diameter at the end of inertial spreading, the drop retraction velocity after maximum spreading and the maximum height reached by the drop centre of mass during rebound. The maximum spreading diameter indicates how much of the initial impact kinetic energy is stored as surface energy as the drop is deformed, while the maximum bouncing height indicates how much energy remains after the impact or, alternatively, can give a measure of the total energy dissipation during impact when subtracted from the impact kinetic energy.

Simple drop impact models on dry surfaces based on energy conservation show that the maximum spreading diameter scales with the Weber number as $D_{\max}/D_0 \sim We^{1/2}$ or, more precisely (Rein 2003):

$$\frac{D_{\max}}{D_0} = \sqrt{\frac{\alpha^2}{6} We + 2} \tag{18}$$

where $\alpha = v_i/v_r$ is the ratio between the rebound and the impact velocities (restitution coefficient). An alternative approach suggests that for $We > 1$ and negligible viscous dissipation, the momentum equation combined with volume conservation yields $D_{\max}/D_0 \sim We^{1/4}$ (Clanet et al. 2004; Biance et al. 2006). However, the latter approach implicitly assumes that upon impact, the drop deforms like a disc, ignoring the formation of a central lamella surrounded by a toroidal rim, which is observed already at moderate Weber numbers.

The maximum diameter of water and polyethylene solution drops at different concentrations after the inertial spreading is plotted in Fig. 15 as a function of the impact Weber number. As expected, the maximum spreading diameter grows monotonically with the Weber number; however, neither Eq. (18) nor the momentum conservation approach ($D_{\max}/D_0 = We^{1/4}$) provides an accurate prediction of experimental data, although they indeed suggest some scaling when plotted in logarithmic scale (Fig. 15b).

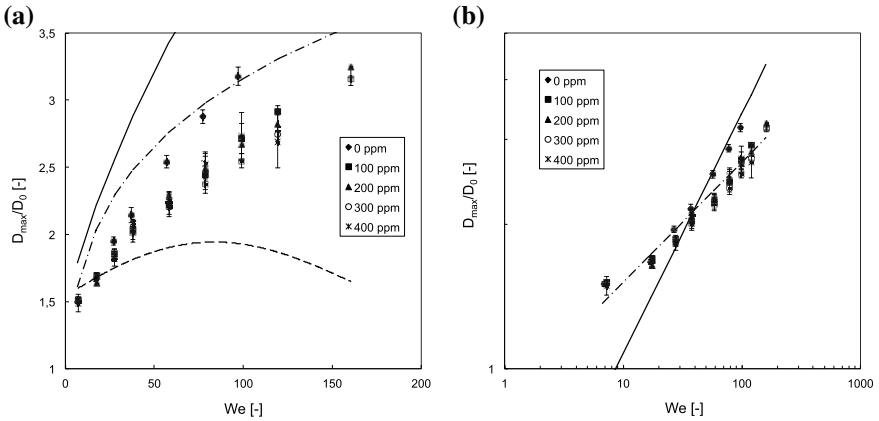

Fig. 15 Maximum spreading diameter of water and polyethylene oxide solution drops at different concentrations with $D_0 \approx 3$ mm impacting on a polished aluminium surface at 400 °C. **a** Linear scale; the dash-dot line corresponds to $D_{\max}/D_0 = We^{1/4}$, while the solid and dashed lines correspond to Eq. (18) with $\alpha = 1$ (no energy dissipation) and $\alpha = v_i/v_r$, respectively. **b** Logarithmic scale; the dash-dot line corresponds to $D_{\max}/D_0 = 0.85We^{1/4}$, while the solid line corresponds to $D_{\max}/D_0 = 0.34We^{1/2}$

For $We \gtrsim 20$, the maximum spreading diameter of viscoelastic drops is systematically smaller than that of water drops having the same impact Weber number, i.e. the fraction of impact kinetic energy (which is proportional to the Weber number) converted into surface energy (which is proportional to the area of the drop surface at maximum spreading) is also smaller. Since the viscosity of polymer solutions is higher than the viscosity of the solvent (in this case, water), the viscous dissipation during the inertial spreading stage is higher in polymer solution drops, hence the observed reduction of the maximum spreading diameter. However, this does not exclude that the surface energy difference between Newtonian and viscoelastic drops at maximum spreading may be stored (at least partially) elsewhere, for example, as elastic energy.

The total energy dissipation during impact and rebound can be obtained from the difference between the drop release height, $H_0 = v_i^2/2$ mg, and the maximum bouncing height, $H_{\max} = v_r^2/2$ mg. During rebound, surface energy is converted back to kinetic energy and propels the drop off the surface; thus, the maximum height of the drop centre of mass allows one to calculate the fraction of surface energy recovered as mechanical energy during rebound. Figure 16 shows that for $We \gtrsim 40$, the maximum bouncing height of viscoelastic drops is significantly larger than that of Newtonian drops, irrespective of the polymer concentration (Bertola 2014) and of the drop diameter (Bertola 2009b), whereas for $We \lesssim 40$ differences are not significant. This shows viscoelastic drops can recover a higher fraction of the initial impact kinetic energy even if they store less in the form of surface energy.

Although these results are consistent with a scenario where the fluid elasticity causes higher rebounds in polymer solution drops, a comparison with shear-thinning

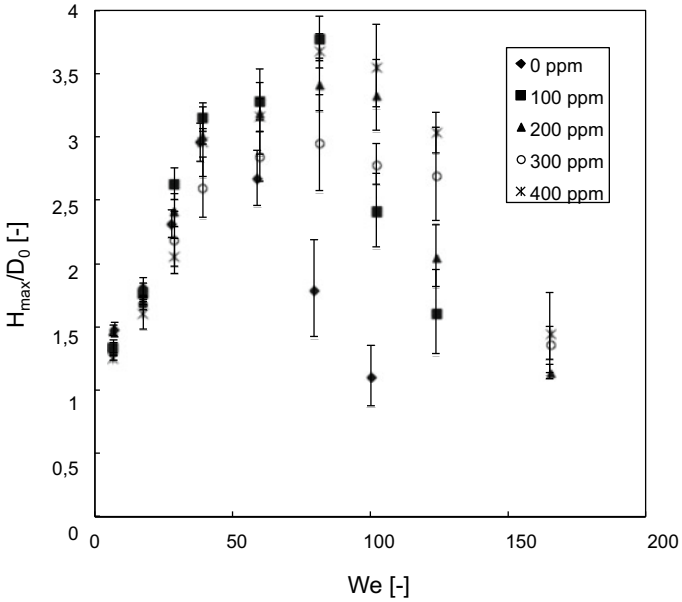

Fig. 16 Maximum bouncing height of water and polyethylene oxide solution drops at different concentrations with $D_0 \approx 3$ mm impacting on a polished aluminium surface at 400 °C

drops, where the fluid elasticity is negligible, demonstrated this interpretation is not correct. In fact, shear-thinning drops bounce much higher than polymer solution drops, even when they have a larger shear viscosity, as shown in Fig. 17 (Black and Bertola 2013).

A more systematic comparison of Newtonian, shear-thinning and viscoelastic drops with matching flow curves revealed that high rebounds (i.e. high restitution coefficients) are axisymmetric throughout the process, while low bouncing heights are observed whenever the rebound is not axisymmetric (Chen and Bertola 2016b). Examples of the drop morphology during rebound for the three fluids considered are displayed in Fig. 18a–c, which shows that while the higher viscosity viscoelastic and shear-thinning drops preserve axisymmetry during rebound, the lower viscosity water drop exhibits non-axisymmetric oscillations. The symmetry breaking observed in lower viscosity water drops is related to the formation of finger-like protrusions on the rim during impact (Fig. 18d), which indicate the onset of the well-known rim instability eventually leading to splashing (Rein 1993; Yarin 2006). These protrusions grow during the inertial spreading stage, and form an axisymmetric crown at maximum spreading; however, at the onset of recoil one can observe that some of the protrusions coalesce to create bigger fingers during retraction, while others do not. Thus, the mass distribution in the retracting droplet becomes non-uniform, which induces asymmetries both in the drop shape and in the internal flows, and eventually causes the drop to rotate around its centre of mass during rebound.

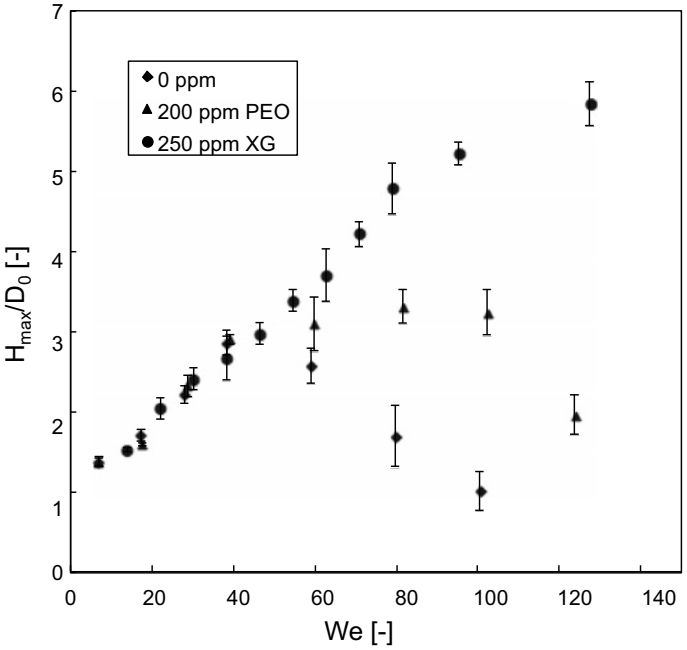

Fig. 17 Comparison of the maximum bouncing heights of water, polyethylene oxide (PEO) solution and xanthan gum (XG) solution drops with $D_0 \approx 3$ mm impacting on a polished aluminium surface at 400 °C

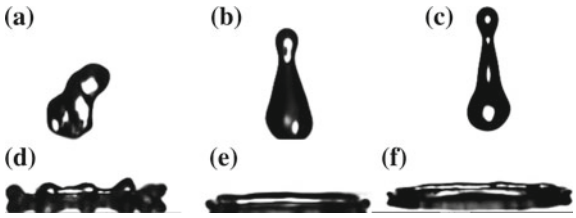

Fig. 18 Rebound morphology of **a** water, **b** 200 ppm polyethylene oxide solution, and **c** 250 ppm xanthan gum solution drops with $D_0 \approx 3$ mm impacting on a polished aluminium surface at 400 °C. The symmetry breaking during the water drop rebound is related to the formation of a crown during impact, which is not observed for the other fluids (**d**–**f**)

When drops exhibit axisymmetric oscillations during rebound (Fig. 18b, c), their kinetic energy converts periodically into surface energy and vice versa, with some dissipation depending on the fluid viscosity. However, if oscillations are not axisymmetric and the drop rotates around its centre of mass (Fig. 18a), a significant part of the kinetic energy is used to sustain the rotation reducing the maximum bouncing height. The rotational kinetic energy of tumbling drops can be estimated as follows:

$$E_{rot} = \frac{1}{2} I \omega^2 \tag{19}$$

where I is the moment of inertia; assuming the elongated drop can be approximated as a cylinder, one obtains

$$I = m\left(\frac{R^2}{4} + \frac{l^2}{12}\right) = \frac{1}{72}\pi\rho D_0^5 \left(\frac{1+2k^3}{2k}\right) \tag{20}$$

where $l = kD_0$ is the cylinder length, measured from images, and R is the cylinder radius, calculated imposing volume conservation.

Since the rotational kinetic energy is not recoverable as potential energy, its value per unit weight must correspond to the bouncing height reduction observed in tumbling drops with respect to drops with the same rheology (viscosity, flow curve) that remains axisymmetric during rebound:

$$\frac{\Delta h}{D_0} = \frac{E_{rot}}{mgD_0} = \frac{D_0\omega^2}{24g}\left(\frac{1+2k^3}{2k}\right) \tag{21}$$

where ω denotes the mean angular velocity and g denotes the gravity acceleration.

Figure 19 compares the maximum bouncing heights of Newtonian, shear-thinning and viscoelastic drops of fluids with matching flow curves. In particular, the viscosity of Newtonian fluids corresponds to the infinite-shear rate and the zero-shear rate viscosities of the non-Newtonian fluids, obtained by fitting the flow curve with the Carreau–Yasuda model (Chen and Bertola 2016b). The bouncing heights of non-Newtonian drops and of the Newtonian drop with viscosity equal to the zero-shear rate viscosity are almost identical, while the bouncing height of the Newtonian drop

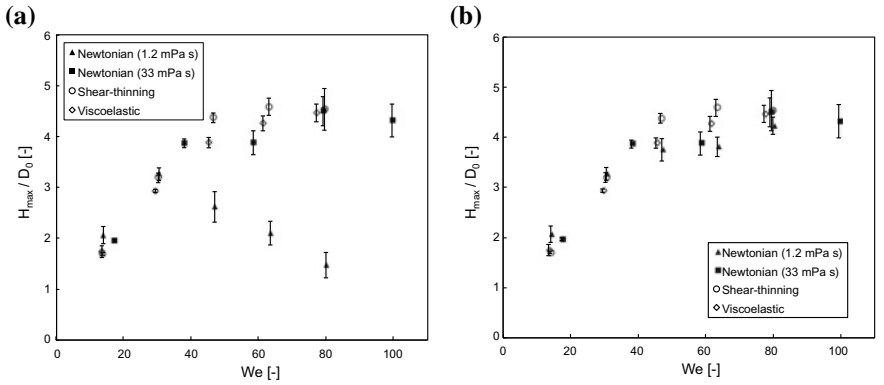

Fig. 19 Maximum bouncing height of Newtonian drops (glycerol solutions), shear-thinning drops (100 ppm xanthan gum solution), viscoelastic drops (80 ppm polyacrylamide solution) with $D_0 \approx 3$ mm impacting on a polished aluminium surface at 400 °C: **a** measured heights; **b** measured heights corrected for the rotational kinetic energy (Eq. 21)

with viscosity equal to the infinite-shear rate viscosity is significantly smaller, similar to water drops in Figs. 16 and 17. However, when the bouncing height of the low-viscosity drop is corrected adding the contribution of the rotational kinetic energy (Eq. 21), it becomes almost identical to the bouncing heights of non-Newtonian drops, as shown in Fig. 19b.

This suggests that the maximum bouncing height (i.e. the restitution coefficient), corresponding to the fraction of the impact kinetic energy recovered after impact, is not affected by non-Newtonian effects, but depends essentially on the zero-shear rate viscosity (i.e. on the viscous dissipation) and on the drop symmetry during rebound. In particular, tumbling drops cannot recover the rotational kinetic energy, and therefore display a significantly smaller bouncing height.

Other impact regimes Besides the conventional impact regimes observed in Newtonian drops (Bertola 2015), dilute polymer solution drops may exhibit other impact morphologies, depending on the Weber number, the impact surface temperature, the polymer concentration and molecular weight. At low polymer concentrations, there is a range of Weber numbers where a single satellite drop separates in the vertical direction during rebound, shortly after the drop has bounced off the surface; this drop is tethered to the main drop body by a thin liquid filament, which is subject to uniaxial stretching, and does not break up until the two droplets re-coalesce into a single drop, as shown in Fig. 20. The diameter of the single satellite drop is between 40 and 50% of the equilibrium drop diameter, D_0; this means that the mass of the satellite drop is about 10 of the total mass of the drop, and therefore the equivalent drop diameter of the drop after the satellite droplet separation is about 96% of the initial equilibrium diameter.

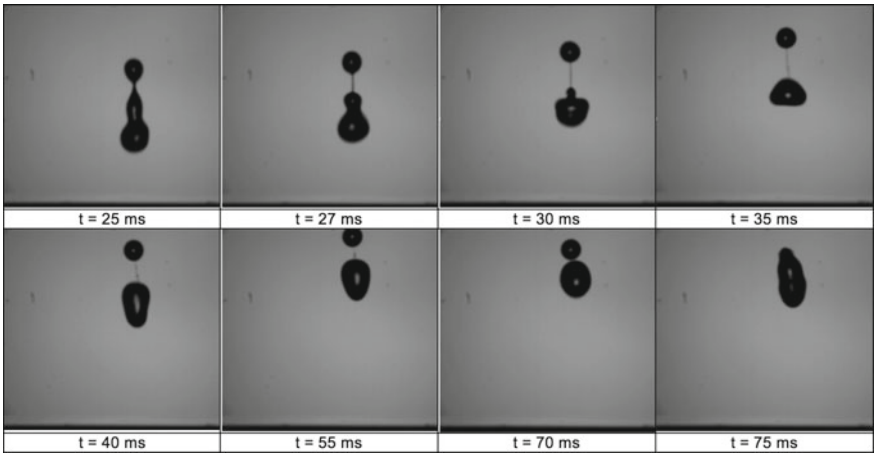

Fig. 20 Single satellite drop morphology observed during the impact of a PEO solution drop (concentration: 100 ppm; molecular weight: 4 MDa) impacting on a surface at T = 400 °C with We = 80; the time origin is the moment of impact

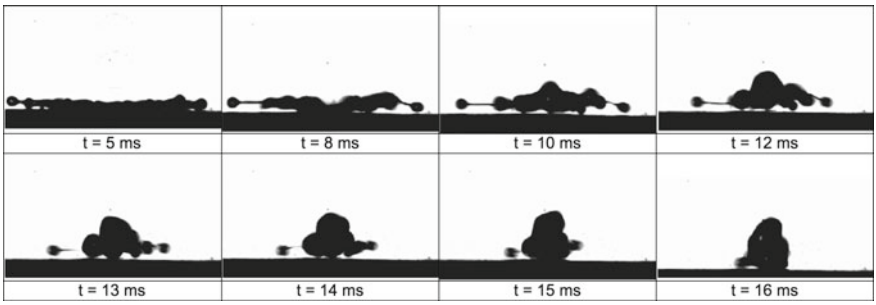

Fig. 21 Semi-splash morphology observed during the impact of a PEO solution drop (concentration: 300 ppm; molecular weight: 4 MDa) impacting on a surface at time origin is the moment of impact

A second impact morphology peculiar of polymer solution drops can be observed at high Weber numbers. When the drop reaches maximum spreading, satellite droplets are formed around the disc perimeter due to the rim instability; in Newtonian drops, this instability eventually evolves into drop splashing. In the case of polymer solutions, a liquid bridge prevents the separation of the satellite droplets from the lamella, as shown in Fig. 21; although the stretching of the liquid bridge is less than in the case of the single satellite drop filament, its elasticity is sufficient to recall the satellite droplets and prevents splashing or breakup. This impact morphology is not observed in Newtonian drops, and can be labelled as *partial splashing* (or *semi-splashing*).

The formation of liquid bridges preventing the separation of satellite droplets also affects the secondary atomisation regime, as shown in Fig. 22. In this case, satellite droplets are sprayed out of the spreading drop free surface due to the bursting of vapour bubbles produced at nucleation sites on the impact surface; however, shortly after their ejection, all satellite droplets forming the spray are pulled back into the main drop, and hence this morphology can be labelled *semi-spray*. The phenomenon has an overall duration of a few milliseconds, and therefore it is very difficult to detect and analyse.

Figure 23 shows the impact regime map relative to a dilute PEO solution with concentration of 200 ppm and molecular weight of the PEO of 4 MDa. In the range of parameters considered, the impact regimes observed are secondary atomisation (SA), rebound with secondary atomisation (RSA), dry rebound (R) and semi-spray (R*). Thus, the map is significantly different with respect to the map obtained for drops of pure water (Bertola 2015); the dominant impact morphology, observed for most combinations of surface temperature and Weber number, is dry rebound, meaning that the polymer additive strongly inhibits both secondary atomisation and splashing.

The effect of polymer concentration is clearly seen upon comparing the map in Fig. 23 with the impact regime maps for a molecular weight of 4 MDa and PEO concentrations of 100 and 400 ppm, displayed in Fig. 24. Reducing the polymer concentration increases the number of different impact morphologies, while for the

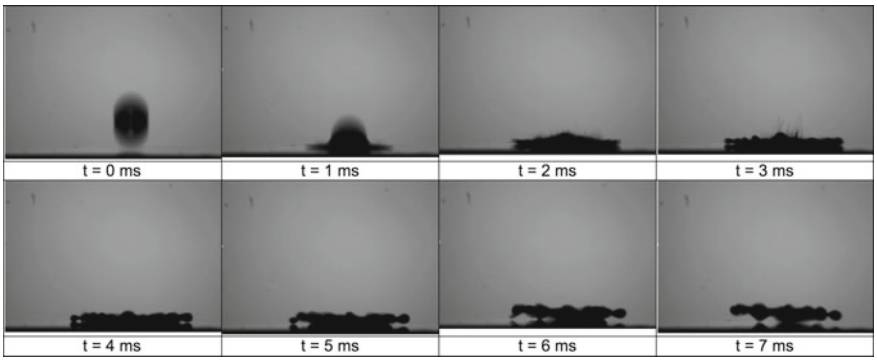

Fig. 22 Semi-spray morphology observed during the impact of a PEO solution drop (concentration: 200 ppm; molecular weight: 4 MDa) impacting on a surface at T = 250 °C with We = 100; the time origin is the moment of impact

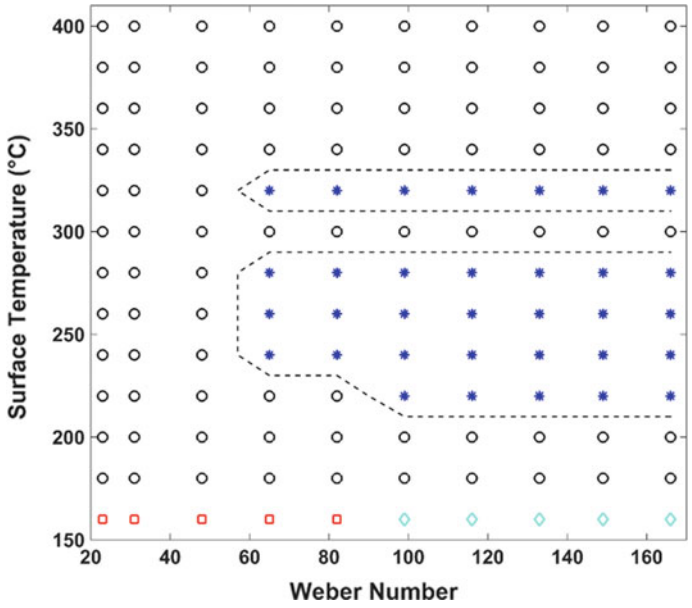

Fig. 23 Impact regime map obtained for a concentration of 200 ppm and a molecular weight of 4 MDa; regimes shown: SA (□), RSA (◇), R (○) and R* (∗)

higher polymer concentration, dry rebound is observed almost everywhere, with the semi-spray regime confined to a small region. Upon keeping the molecular weight constant at 4 MDa and gradually increasing the concentration from 100 to 200 ppm, all breakup and splashing are completely overcome; with the exception of small-scale secondary atomisation which is prevalent at a surface temperature of 160 °C. However, upon increasing the concentration to 400 ppm, no secondary atomisation

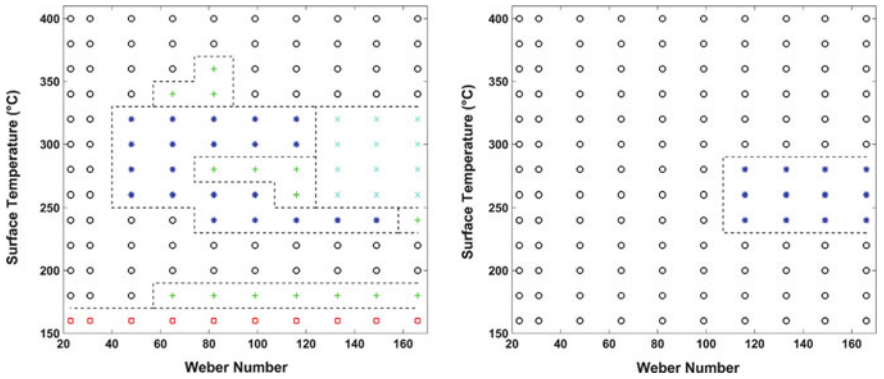

Fig. 24 Impact regime maps obtained for a molecular weight of 4 MDa at concentrations of 100 ppm (left) and 400 ppm (right); regimes shown: SA (□), B (+), R (○), R* (∗) and S (×)

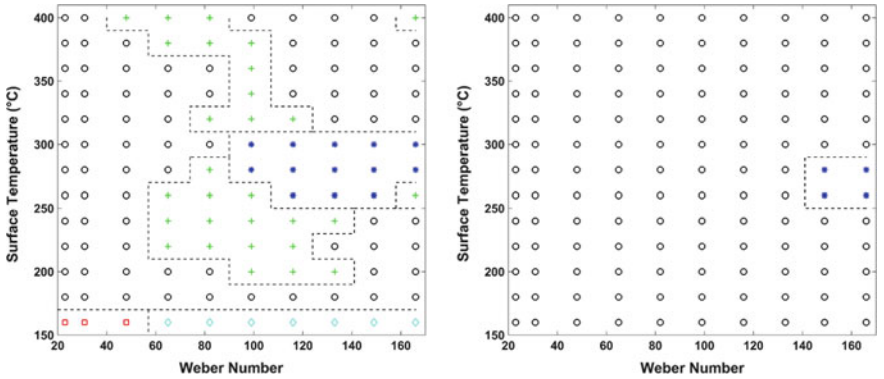

Fig. 25 Impact regime maps obtained for a concentration of 200 ppm and molecular weights of 2 MDa (left) and 8 MDa (right); regimes shown: SA (□), B (+), R (○), R* (∗) and S (×)

is observed even at surface temperature of 160 °C. For all surface temperatures considered, rebound is the primary impact outcome.

Similarly, the effect of the molecular weight of the polymer can be seen upon comparing the map in Fig. 23 with the impact regime maps for a concentration of 200 ppm and molecular weights of 2 MDa and 8 MDa, displayed in Fig. 25. Within the 2 MDa (200 ppm) impact regime map, secondary atomisation (SA), rebound with secondary atomisation (RSA), rebound (R), semi-spray (R*) and drop breakup (B) regimes are observed. Upon gradual increase of molecular weight from 2 MDa to 4 MDa, the breakup regime is completely suppressed; however, some secondary atomisation is still present at a surface temperature of 160 °C. Increasing the molecular weight to 8 MDa, all secondary atomisation is completely suppressed.

Thus, from a qualitative standpoint, the effect of molecular weight is similar to that of the polymer concentration; low molecular weights enable the development of

different impact morphologies, while increasing the molecular weight progressively suppresses secondary atomisation and breakup/splashing, until only the dry rebound regime can be observed.

The similarity between the effects of the molecular weight and of the polymer concentration on the impact morphology is justified because both of these parameters affect the relaxation time of polymer solutions (Kalashnikov and Askarov 1989). When the relaxation time is shorter than the characteristic hydrodynamic timescales corresponding to the various impact morphologies, the effect of the polymer additive is negligible; however, when the relaxation time and the hydrodynamic timescales are of the same order, the behaviour of polymer solutions becomes significantly different from that of the pure solvent.

3 Impact of Viscoplastic Drops on Solid Surfaces

3.1 Impact on Homothermal Surfaces

Although viscoplastic (or yield stress) fluids have been studied for about one century, and despite their relevance in several applications, the first investigation of yield-stress drops was published only recently (Nigen 2005). This work studies the impact of a model viscoplastic fluid (Vaseline) on a plexiglass surface, for different impact velocities. The rheological behaviour of the fluid was described using a Cross model, modified to include a yield-stress component. The variation of the final drop shape with respect to the impact velocity was characterised with respect to the Bingham number, $Bm = \tau_0 D_0/\mu_0 v_i$, where v_i is the impact velocity and μ_0 is the zero-shear rate viscosity; however, such definition is not well posed because whilst the Bingham number characterises the ratio of viscous to yield-stress forces, viscous dissipation only occurs during fluid motion, and therefore the Bingham number definition given above is only valid at zero-shear rate, i.e. when the drop is at maximum spreading.

Because surface forces play an important role in all drop impact phenomena, it is interesting to observe what happens when the yield-stress magnitude is comparable with the capillary (Laplace) pressure. This leads to the definition of a capillary regime and a viscoplastic regime, which can be characterised through the Bingham-capillary number (Bertola 2009a):

$$\check{B} = \frac{\tau_0 D_0}{\sigma} \tag{22}$$

Whilst in the capillary regime, the impact morphology is qualitatively similar to that of simple liquids, in the viscoplastic regime, one can sometimes observe permanent deformations that do not disappear upon impact or under the action of surface forces. For example, if drops are produced from a capillary nozzle, the prolate shape that is created during the fluid extrusion (Coussot and Gaulard 2005; German and Bertola 2009a, 2010a, b) remains partly visible after impact, as shown in Fig. 26,

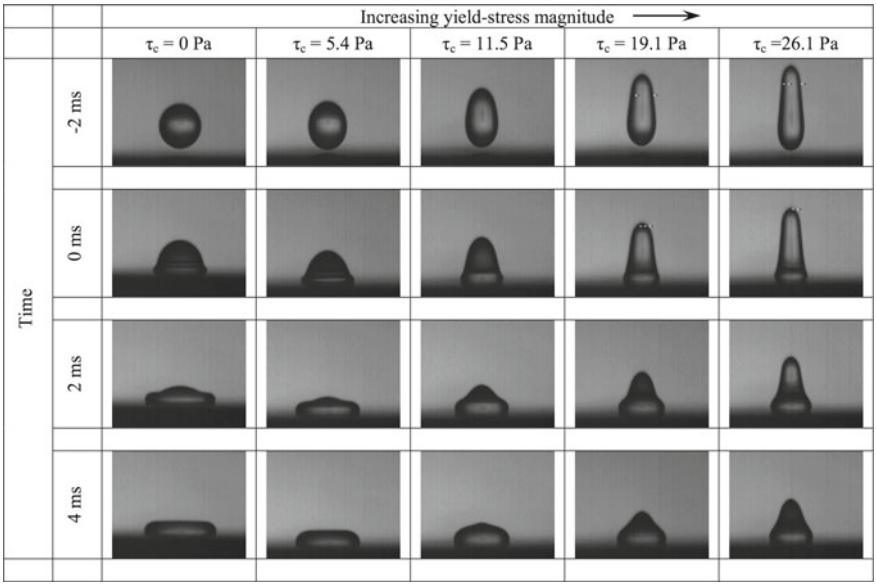

Fig. 26 Base diameter and dynamic contact angle of commercial hair gel (Carbopol gel) drops with different magnitudes of the yield stress and $D_0 \approx 2.5 \div 3$ mm impacting on a hydrophobic surface (Parafilm) from a fall height of 25 mm

which displays the impact morphology of hair gel-water drops for different yield-stress magnitudes. This phenomenon is also influenced by inertia, and becomes less and less pronounced at higher impact Weber numbers. The droplets symmetry can be improved significantly if the dispensing nozzle has a very small diameter (Saidi et al. 2010); however, for high yield-stress magnitudes and low impact velocities, drops still preserve the initial shape they have after detachment from the capillary.

In viscoplastic drops, the maximum spreading diameter at the end of inertial spreading decreases linearly with the yield-stress magnitude (German and Bertola 2009a), while in Newtonian drops, the same quantity depends on viscosity according to a power law (Rein 1993; Chandra and Avedisian 1991; German and Bertola 2009b), as shown in Fig. 27.

The influence of surface wettability on viscoplastic drop impacts is only noticeable after the end of the inertial expansion stage. In the viscoplastic regime ($\check{B} > 1$), drops impacting on hydrophobic surfaces exhibit only small retractions similar to those observed for high-viscosity Newtonian fluids; impacts on hydrophilic surfaces show no significant retraction, and slow capillary-driven spreading follows directly on from the fast spreading of inertial expansion at low impact velocities. At higher Weber numbers, drop diameters remain nearly constant after maximum spreading (German and Bertola 2009a). These results are substantially confirmed by a more detailed study of the effect of surface wettability and roughness on viscoplastic drop impacts (Saïdi et al. 2011), which compares two smooth substrates with distinct surface energies

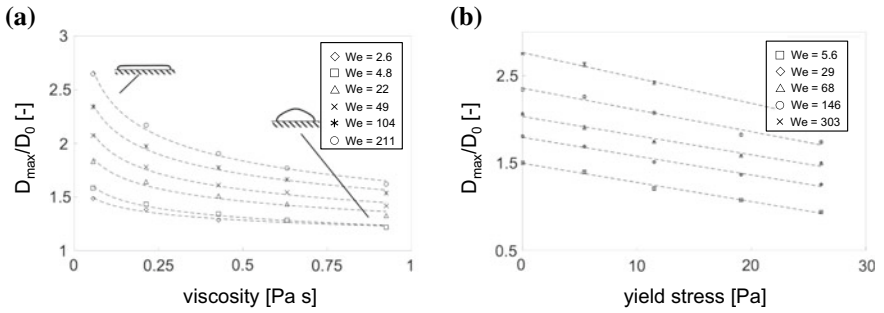

Fig. 27 Maximum spreading diameters of Newtonian glycerol–water mixture (**a**) and viscoplastic commercial hair gel (Carbopol gel) drops (**b**) impacting on a hydrophobic surface (Parafilm). Adapted from German and Bertola (2009a)

and three substrates with similar surface energy but different roughness. The same work also attempts at a quantification of the effects of apparent wall slip (Bertola 2009a; Barnes 1995) on drop impact, however without being conclusive since it was not possible to disentangle the effects of wall slip and surface wettability during experiments. It is speculated that at low inertia, where a gravitational subsidence is observed, the creeping movement amplitude is governed by interfacial effects rather than wall slip, while at high impact velocities, wall slip effects become appreciable only in the last moments of the recoil, when shear rates become very low.

When the drop radius is much larger than the capillary length, $a = \sqrt{\sigma/\rho g}$, surface tension effects can be neglected in comparison with those of gravity; furthermore, large diameters also imply large Weber numbers, so that impacts are dominated by inertia and by the rheological properties of the fluid only. Such experimental conditions are explored in a recent work, which describes the impact of relatively large bits (characteristic sizes between 10 and 30 mm) of various viscoplastic fluids, with yield-stress magnitudes ranging from 4 to 124 Pa, and capillary lengths of the order of a few millimetres (Luu and Forterre 2009). Although these fluids include many aqueous Carbopol dispersions, it must be observed that their yield-stress magnitudes are significantly smaller than the values reported in the open literature for Carbopol dispersions with the same concentrations (Rogers and Barnes 2001). This suggests the Carbopol dispersions used in that work were not prepared following the standard protocol which prescribes fluid neutralisation to ensure it has the highest yield-stress magnitude.

By comparing impacts on a glass surface and on a superhydrophobic surface (contact angle of nearly 180°), these experiments confirm that the maximum spreading diameter of viscoplastic drops is weakly dependent on the surface wettability, and smaller than the capillary limit as defined by Saïdi et al. (2011); unfortunately, similar results are also obtained with high-viscosity Newtonian fluids (German and Bertola 2009b), so that it is not possible to establish whether the yield stress has an independent influence. The most interesting finding of this work is the strong and rapid recoil, which may even be followed by a complete rebound, observed after

the spreading phase of Carbopol drops impacting on the superhydrophobic surface. Since both a recoil driven by surface tension and a purely elastic rebound (the flow threshold corresponds to a shear deformation of about 25%, whereas deformations during impact vary between 100 and 500%) must be ruled out, it is suggested that at such high velocity gradients ($We \approx 1400$) Carbopol dispersions may exhibit a viscoelastic behaviour: during the rapid spreading phase, the flow is faster than the fluid relaxation time, resulting in giant elastic deformations on short timescales. This conjecture is supported by the comparison of experimental results with a minimal model of elasto-viscoplastic inertial spreading, where elasticity is tentatively accounted for by the storage modulus measured below the flow threshold (indeed, a very rough approximation). However, it appears that in order to obtain independent evidence in support of this picture, dynamic rheometric tests with characteristic frequency comparable with the inverse of the impact timescale are necessary.

3.2 Impact on Heated Surfaces

The study of viscoplastic drops impacting on heated surfaces is limited to the case of Leidenfrost drops (Chen and Bertola 2016a). In this context, the Leidenfrost drop impact represents a model system to investigate the behaviour of a viscoplastic fluid where the yield stress is of the same order of magnitude as the Laplace pressure in the absence of wetting.

At the end of the inertial spreading following impact, the liquid lamella is static (i.e. there is no inertial force); thus, retraction results from the competition between the driving surface tension forces (or the Laplace pressure) and the resisting yield stress, and can be expressed in terms of the Bingham-Capillary number, $\check{B}$, defined in Eq. (22). At low values of the Bingham-capillary number ($\check{B} < 1$), the Laplace pressure exceeds the yield stress, and therefore the drop recoils to restore the spherical shape minimising the surface energy; however, for $\check{B} \gtrsim 1$, the surface tension can no longer overcome the yield stress, and causes only little retraction resulting in

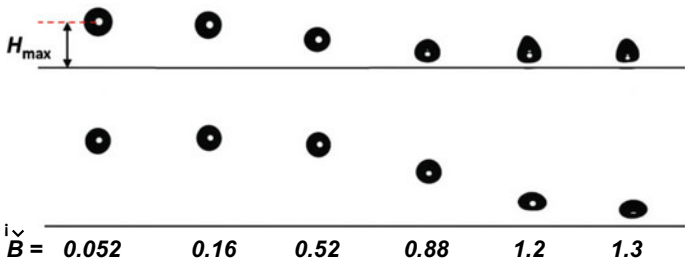

Fig. 28 Images of Carbopol gel drops with $D_0 \approx 3$ mm at maximum bouncing height after impacting on a polished aluminium surface at 400 °C, for different magnitudes of the yield stress and **a** $We \approx 15$ and **b** $We \approx 110$

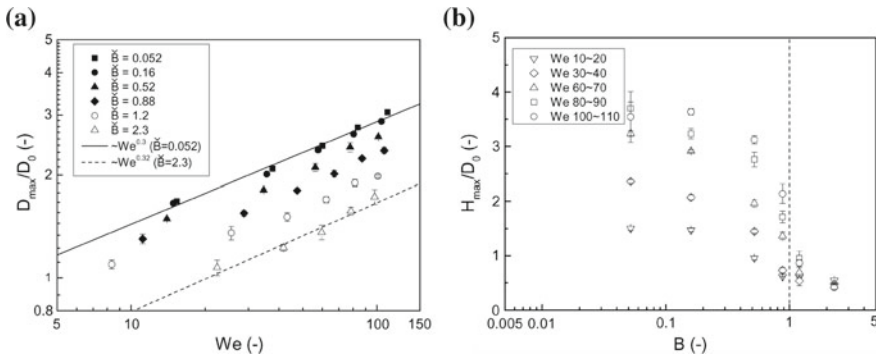

Fig. 29 Maximum spreading diameter (**a**) and maximum bouncing height (**b**) of viscoplastic drops with $D_0 \approx 3$ mm impacting on a polished aluminium surface at 400 °C, for different magnitudes of the yield stress and different impact Weber numbers (Chen and Bertola 2016a)

an oblate drop shape. Consequently, rebound is possible only when $\breve{B} < 1$, and not when $\breve{B} \gtrsim 1$, as shown in (Fig. 28), which displays images of viscoplastic drops at maximum bouncing height for different values of $\breve{B}$, for the same impact Weber number.

The maximum spreading diameter, which is proportional to the surface energy of the drop at the end of spreading, hence it can be used to estimate the energy dissipation during the spreading process for a given initial kinetic energy of the drop, which is displayed in Fig. 29a as a function of the impact Weber number. For a given magnitude of the yield stress (i.e. for a given $\breve{B}$), the maximum spreading diameter scales approximately as $D_{max}/D_0 \sim We^{1/3}$, which is in between the scalings resulting from energy conservation ($D_{max}/D_0 \sim We^{1/2}$) and momentum conservation ($D_{max}/D_0 \sim We^{1/4}$). The maximum spreading diameter decreases monotonically with respect to the Bingham-capillary number since larger values on the yield stress cause larger viscous dissipation of energy.

The maximum bouncing height of the drop centre of mass during rebound, which indicates how much of the initial impact kinetic energy remains after the impact, hence it can be used to calculate the total energy dissipation during impact when subtracted from the impact kinetic energy, which is displayed in Fig. 29b as a function of the Bingham-capillary number. For drops with a relatively low yield stress ($\breve{B} = 0.052$; $\breve{B} = 0.16$; $\breve{B} = 0.52$), the rebound behaviour is similar to high-viscosity Newtonian drops. When the yield stress is larger than the Laplace pressure ($\breve{B} = 1.2$; $\breve{B} = 2.3$), the rebound behaviour of drops becomes totally different from the others, and the maximum bouncing height is equal to $0.5D_0$ within experimental error; in addition drops keep a permanent deformation resulting into an oblate shape.

Although the rebound of Leidenfrost drops is usually explained as a consequence of the rapid release of the surface energy stored during inertial spreading, similar to drop rebound on non-heated, hydrophobic surfaces, where there is no vapour film, some authors suggest that the rebound is also due to the formation of a high-pressure

vapour layer between the liquid and solid surface during impact, which acts as an elastic cushion which contributes to propelling the drop off the surface (Rein 2003). However, according to the above results, drops do not rebound when surface forces cannot restore the spherical shape, and therefore one must conclude the contribution of the vapour cushion to rebound is negligible.

4 Atomisation of Non-Newtonian Fluids

In many technical applications, fluids atomised are non-Newtonian in their response to deformation. Examples are paints used for coating purposes and polymer solutions in spray drying processes for polymer powder production. Other fields of application are crop spraying in agriculture, where polymeric compounds are used to suppress the formation of very small drops (anti-drift agents), and rocket propulsion, where solid propellants are being replaced by gel-like fluids. The advantage of such propellants is that they are similarly shelf-stable as solids, while thrust is controllable, which is not the case with solid propellants. In all cases, it is important to predict the drop size spectrum produced by the atomisation process, which depends both on the atomiser and its state of operation, and on liquid material properties. In most cases, the viscous or elastic properties of the liquid depend on the rates of deformation, where viscoelastic liquids may exhibit a memory effect, so that their material properties may additionally depend on the deformation history.

In this section, we first present a review of published research on spray formation from non-Newtonian liquids (Brenn and Plohl 2017).

4.1 Non-Newtonian Jet Breakup and Spray Formation

We first discuss the breakup of laminar jets of non-Newtonian liquids. Mun et al. (1998) showed that in laminar capillary jet breakup, both the breakup length of the jet and the size of the main and satellite drops formed are functions of the concentration and the molecular weight of the polymer in the solution. The authors investigated solutions of poly(ethylene oxide) (PEO) in mixtures of water and glycerol. The composition of the solvent was designed so as to maintain a constant shear viscosity of 5 mPa·s for all the experiments. The extensional viscosity of the liquids, represented by the Trouton ratio, was determined with an opposing-jets rheometer. The experiments showed that, at low molecular weight of the order of 8–100 kDa and low concentration of the polymer between 0.1 and 1 wt%, the jet may be destabilised by the dissolved substance. At higher molecular weight, the jet breakup length increases with the polymer concentration and reaches a plateau. These results explain the different trends in jet breakup length found by Kroesser and Middleman (1969) and by Goldin et al. (1969). Drop size measurements show that the formation of satellites is suppressed only when the jet breakup length increases due to the dissolved polymer.

The increase of drop size due to the polymer is explained by the formation of fewer drops with fluids showing larger breakup lengths.

The breakup of laminar viscoelastic liquid jets was further studied by Christanti and Walker (2001). The jets are produced by a Spraying Systems twin-fluid atomiser without an airflow, essentially using the cylindrical tube in the atomiser for liquid supply to the orifice. The liquid flow rate was kept constant throughout the experiments, with a jet velocity of about 2 m/s and a jet diameter of about 500 μm. The liquids were the glycerol–water mixtures with dissolved PEO of Mun et al. (1998), where three different molecular weights of the polymer and mass fractions up to 0.3% were studied. The extensional viscosity of the solutions was again characterised by an opposing-jets rheometer. The jet breakup experiments show that the polymer content delays the onset of jet surface deformation and, due to the formation of the beads-on-a-string structure, raises the breakup length considerably, up to more than a factor of two as compared to the Newtonian case. Drop size distributions show that the main and satellite drop sizes on average agree with predictions by Rayleigh (1878) and by Bousfield et al. (1986), respectively. Drop size spectra do not change significantly as the concentration of PEO with the molecular weight of 300 kDa is increased from 0.1% to 0.33%. Drop formation from solutions of two different molecular weight PEOs shows to be dominated by the PEO with the higher molecular weight. The smaller PEO helps to suppress the formation of small-size drops. The stretching rates are attempted to be estimated but do not lead to a characterisation of the drop sizes formed as functions of characteristic numbers involving the stress relaxation time.

Christanti and Walker (2002) studied the breakup of laminar jets of PEO solutions investigated by Christanti and Walker (2001), going to higher molecular weights of the PEO up to 5000 kDa and applying defined disturbances to the jet. The focus is on the formation of satellite droplets in the jet breakup. Relaxation times of the solutions were determined from the rates of thinning of filaments formed between the main drops in the breakup process. For dilute solutions, the results agree with the prediction from the Zimm model. Satellite droplet formation may be suppressed due to the polymer action, even at small disturbance amplitudes. The drop size distribution may be controlled by the molecular weight of the polymer. The parameter determining the drop formation process is the product of liquid stress relaxation time to the disturbance growth rate.

Teske and Bilanin (1994) investigated sprays produced from Newtonian liquids by various types of atomisers, representing a non-dimensional drop size by means of characteristic numbers. The authors account for the influences from the velocity ratio between liquid and ambient air, the spraying angle, as well as the Reynolds number $Re = U_j D_j \rho/\mu$ (jet velocity and diameter U_j and D_j, liquid density and dynamic viscosity ρ and μ), the ratio of rotary and axial velocities in rotary atomisation, the liquid Weber number $We = U_j^2 D_j \rho/\sigma$ (surface tension σ of the liquid against the ambient air), as well as the liquid Deborah number, which is defined as the ratio $De = \tau_n U_j/D_j$ of time scales of stress relaxation and flow, τ_n and D_j/U_j, and ratio of elastic to viscous stresses $\Pi_s = c_n D_j/(\mu U_j)$ (stress relaxation amplitude c_n, viscous stress $\mu U_j/D_j$). For water sprays, three non-dimensional

characteristic sizes of the cumulative drop size spectrum are represented as functions $A + B\ Re\ We^b$. This correlation is different for rotary atomisation. The values of A and B are found different (A even with different sign) in the different sprays studied, while the exponent b is constant for each atomiser type ($b = 0.42$ for flat-fan and $b = 0.38$ for pressure-swirl atomisers. The correlation is different for every atomiser geometry, represented by the spray opening angle.

A pressure-drop-based method for measuring the extensional viscosity of dilute polymer solutions was presented by Dexter (1996). The solution to be characterised flows through a packed bed of screens, driven by varying pressure difference. The extensional viscosity is derived directly from the ratio of applied pressure difference to the resulting liquid volume flow rate. The pressure drop is assumed to be due to contributions from shear, elongation and inertia. The equation for the extensional viscosity of the polymer solution derived and evaluated by the measurements does not claim to provide accurate values, but rather a measure for it. A correlation between this quantity and the median drop size in the sprays from a Spraying Systems TeeJet flat-fan atomiser shows that the median drop size increases by a factor of 5 due to a tenfold increase of the extensional viscosity. At the same time, the percentage of drops smaller than 102 μm drops from 30 to 1.

Zhu et al. investigated the effectiveness of anti-drift agents used in agricultural pesticide formulations for suppressing small drop size fractions in pesticide sprays (Zhu et al. 1997). In order to simulate the process of liquid flow through atomisers for agricultural applications, the liquids were exposed to shear. Aqueous solutions of different polymers with different molecular weights and anionicities were studied at different concentrations. The high-shear dynamic and extensional viscosities of liquid samples were determined after different numbers of passes through the test piping. The apparatus used for extensional rheometry was the one by Dexter (1996). The liquids were then atomised by a flat-fan pressure atomiser and drop sizes measured with a phase-Doppler anemometer. The liquid rheometry showed a significant decrease in the shear viscosity against the fresh solution after 11 passes through the apparatus. At that state of the liquid, the drop size $D_{v0.5}$ of the cumulative volume distribution in the sprays decreased by 25%. The authors concluded from this finding that formulations containing polymers of the kinds studied increase in susceptibility to drift as the solution passes several times through the sprayer. This effect is partially suppressed with anionic poly(acrylamide)s by increasing the polymer concentration. Increasing the concentration, however, does not help with non-ionic polymers. The reason for this difference is seen in the different conformations of the molecules in the solution.

Mun and co-workers investigate the atomisation of dilute solutions of PEO for four different molecular weights in the same mixtures of glycerol and water as above (Mun et al. 1999). The solutions were supplied at a constant pressure to several Spraying Systems full jet and cone jet nozzles allowing for a constant liquid volume flow rate. The liquids were characterised for their shear and extensional viscosities, as in Mun et al. (1998), and for the surface tension against air. The volume mean drop size in the sprays increases by a factor of 4 due to 0.095 wt% of 600 kDa PEO in the solution. The exact value depends on the atomiser geometry. At the same time,

the content of drops smaller than 105 μm in the sprays decreases by a factor of 5 or more. From these, follow implications on liquid characterisation, agricultural chemical formulation and atomiser design.

The effect of polymer rigidity and concentration on the atomisation of aqueous polymer solutions by a pressure-swirl atomiser was studied by Harrison et al. (1999). The focus of the study is on the opening angle of the spray cone as a function of the concentration of the polymers. The non-monotonous behaviour of the spray cone angle with varying polymer concentration for flexible (poly(acrylamide)), semi-rigid (CMC) and rigid polymers (Xanthan gum) is related to the extensional viscosity of the solutions. The spray cone formation and sheet breakup are enhanced at low polymer concentrations and retarded with increasing concentration. The drop sizes produced are not reported.

Romagnoli et al. (2000) study the spraying of solutions of PEO and hydroxypropyl guar gum (HPG) in water and in aqueous solutions of poly(ethylene glycol). Atomisers were flat-fan TeeJet nozzles from Spraying Systems. The liquid extensional viscosity was rheologically characterised, and their surface tension was measured. Drop sizes were measured with a Malvern instrument at a constant distance from the atomiser orifice. Drop size spectra in sprays from two solutions with very similar extensional viscosities, but surface tensions differing by 17%, are found to be very different. This finding allows for the conclusion that, in the cases investigated, the extensional viscosity is not the most important factor determining the drop size.

In their experiments on viscoelastic fluids atomisation, Thompson and Rothstein (2007) used solutions containing worm-like micelles of CTAB, with sodium salicylate at the same molarity. The nozzles were flat-fan and pressure-swirl atomisers from the company McMaster-Carr. Oscillatory and steady shear rheometry revealed the shear viscosity as a function of the shear rate and the storage and loss moduli as functions of the oscillation frequency. Zero-shear viscosities up to 68 Pa s are reached, accompanied by stress relaxation times of the order of 30 s. For the flat-fan atomisers, the authors present a chart for the pairing of the Weber and elasticity numbers, We and El, of regimes of stable sheet or sheet breakup mechanisms where the elasticity number is defined as $El := \lambda_1 \nu_0 / R^2$ (stress relaxation time λ_1, zero-shear rate liquid kinematic viscosity ν_0, jet radius R) and is $O(10^6)$ in the study. The regimes seem very similar for two atomisers with opening angles differing by a factor of 2. As a dominant breakup mechanism, the formation of perforations in the fan-shaped sheets is found. The corresponding nomogram for the pressure-swirl atomiser accounts for the various shapes of liquid systems formed for varying Weber and elasticity numbers from a jet to a ruptured cone. Drop size dependencies on liquid properties and setting of atomiser operation are not reported.

Williams et al. (2008) investigated the influence of different poly(acrylamide)s dissolved in water at various concentrations on the Sauter-mean drop size in sprays of the solutions produced by an agricultural spray nozzle from Lurmark. The polymers were non-ionic, anionic or cationic. A characterisation of the solutions included shear and extensional rheometry, as well as tensiometry. The Sauter-mean drop size in the sprays was measured with a Malvern Spraytec RS instrument. Bouncing of 1 mm drops impacting an inclined plant leaf at a set velocity was characterised by

the bouncing distance. The polymer solutions exhibited shear-thinning and strain-hardening behaviour. The shear viscosities at low shear rates reported are O(1 Pa s) at polymer concentrations O(0.07 wt%). The flow curves exhibit a hump around shear rates of 500 s^{-1}. The strain hardening is seen by an increase of the apparent extensional viscosity with the Hencky strain. The thinning curves of the filament diameter in the extensional rheometry show a transition from a viscoelastic to a Newtonian behaviour, as seen in other studies also (Stelter et al. 2002a). Spray Sauter-mean drop sizes increase by approximately 10% while the extensional viscosity of the liquid increases by a factor of four.

Park and Harrison (2008) studied the effects of elasticity of the liquid on the performance of the spray produced with a Spraying Systems Turbo TeeJet nozzle. The context is spraying of pesticide formulations and spray painting. An increased extensional viscosity raises the breakup lengths of sheets. In the sheet breakup, filaments connecting the nascent drops are formed. The stability of these filaments leads to increased drop sizes and suppresses the fine droplet fractions in the sprays. The polymer employed was PEO. The solvents used were different mixtures of water and glycerol, and the largest polymer mass fraction in the solutions was 0.6 wt%. The resulting shear viscosity was around 5 mPa for all the solutions studied. The extensional characteristics of the solutions are not reported. The volumetric mean drop diameter in the sprays increases by 40% as 0.6 wt% of PEO with a molecular weight of 100 kDa are added to the Newtonian solvent.

Negri and Ciezki (2015) investigated the spraying behaviour of 13 Boger fluids, with an impinging-jet injector. The application is rocket propulsion with gelled propellants. The formation of spray drops by breakup of liquid sheets formed by the mutual impact of two inclined cylindrical liquid jets is ligament mediated. For characterising the ligaments, the authors defined a thread parameter as the ratio of the sum of the third powers to the sum of the second powers of the major axis lengths of the filaments visualised in the process. The definition, therefore, is analogous to that of a Sauter-mean drop diameter. It is assumed that the thread parameter is relevant for quantifying the drop size distribution in the spray. The data show that the thread parameter is correlated with the stress relaxation time of the Boger fluids. It is shown that the elasticity number $El = \lambda_1 \nu / D_j^2$ (liquid kinematic viscosity ν, jet diameter D_j), representing the ratio of the stress relaxation time to a viscous diffusive timescale, correlates well with the thread parameter. The thread parameter itself, however, is presented in dimensional form.

The group of Keshavarz et al. (2015) studied the formation of drops in an air-assisted spraying process of aqueous PEO solutions with dynamic shear viscosities around 3 m Pa s, polymer mass fractions between 0.01 and 0.1% and small molecular weights between 300 and 1000 Da. Careful extensional rheometric characterisation of the solutions includes the presentation of a jet-thinning-based method originally proposed by Schümmer and Tebel (1983), now called ROJER. This method allows the stress relaxation time even of dilute solutions to be measured, where the limitations of the CaBER method do not allow this. Findings by Marmottant and Villermaux (2004), as well as estimates on time to breakup of a filament producing the drops and a time scale characteristic for the influence from the atomising air, lead to a

correlation of the mean drop size with the influencing characteristic numbers We, Oh and De. Here, $Oh = \mu/(\sigma D\rho)^{1/2}$ is the Ohnesorge number, representing a ratio of a capillary to a viscous timescale. The accuracy of predictions of this model remains to be verified. We name this paper despite the twin-fluid atomisation process since it presents a mean drop size model.

In the following, we discuss the instability of liquid jets and sheets formed for producing sprays by well-known types of atomisers. For reasons of relevance for the application, we then go into the details of spray formation by sheet breakup.

4.2 Instability of Non-Newtonian Jets and Sheets

Due to the instability of jets and sheets in contact with an ambient gaseous medium, deformations of the free surface of the liquid system, which are caused by dynamic influences, may grow either in space or time, or both. The deformations, therefore, lead to the breakup of the system into drops. The mechanism of instability may be either capillary (the Rayleigh mechanism), due to a tangential acceleration of the gas–liquid interface (the Kelvin–Helmholtz mechanism), or due to a normal acceleration of the interface (the Rayleigh–Taylor mechanism), or due to more than one of these mechanisms. For jets, we concentrate our discussion on the capillary instability, while for sheets, we look at the Kelvin–Helmholtz mechanism. We discuss details of the linear stability analysis of jets and sheets in a vacuum and in a gaseous ambient medium, respectively.

Linear stability analysis of a laminar liquid jet We sketch the linear temporal capillary instability analysis of a liquid jet. The jet is assumed to be axisymmetric around the z-axis of the cylindrical coordinate system. The liquid is treated as incompressible and linearly viscoelastic. Dynamic influences from an ambient medium, as well as body forces, are not accounted for.

The jet surface in Fig. 30 is described as $r_s(z,t) = a + \eta(z,t)$, where η is the deformation against the undisturbed cylinder of radius a. The variables and equations of change are non-dimensionalised with the undeformed jet radius a, the capillary timescale $(\rho a^3/\sigma)^{1/2}$, the capillary pressure σ/a and the reference stress

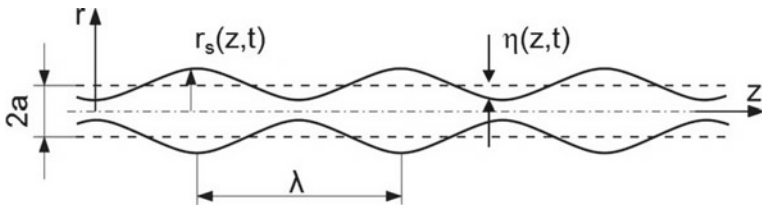

Fig. 30 Surface of an axially symmetric capillary jet with sinuous deformation of wavelength λ

$\mu_0(\sigma/\rho a^3)^{1/2}$ for length, time, pressure and extra stress, respectively. Here, ρ is the liquid density, σ is the surface tension and μ_0 is the liquid zero-shear viscosity.

For the problem at hand, the linearised equation of continuity and the two linearised components of the momentum equation in the radial (r) and axial (z) directions read

$$\frac{1}{r}\frac{\partial}{\partial r}(ru_r) + \frac{\partial u_z}{\partial z} = 0 \tag{23}$$

$$\frac{\partial u_r}{\partial t} = -\frac{\partial p}{\partial r} + Oh_0\left[\frac{1}{r}\frac{\partial}{\partial r}(r\tau_{rr}) - \frac{\tau_{\theta\theta}}{r} + \frac{\partial \tau_{rz}}{\partial z}\right] \tag{24}$$

$$\frac{\partial u_z}{\partial t} = -\frac{\partial p}{\partial z} + Oh_0\left[\frac{1}{r}\frac{\partial}{\partial r}(r\tau_{rz}) + \frac{\partial \tau_{zz}}{\partial z}\right] \tag{25}$$

where $Oh_0 = \mu_0/(\sigma a\rho)^{1/2}$. As the rheological constitutive equation (RCE), we use the linearised form of the Oldroyd-B model, which reads

$$\tau + De_1\frac{\partial \tau}{\partial t} = 2\left(D + De_2\frac{\partial D}{\partial t}\right) \tag{26}$$

where the symbols τ and D denote the extra-stress and the rate-of-deformation tensors, respectively. De_1 and De_2 are the Deborah numbers corresponding to the stress relaxation and deformation retardation times, λ_1 and λ_2, respectively.

This set of equations is solved subject to linearised boundary and initial conditions. The first boundary condition is the kinematic condition that the radial rate of deformation of the jet surface equals the radial velocity component evaluated at the position of the undeformed cylindrical jet. The second condition is the dynamic condition stating that there is no transfer of shear stress across the jet surface. The third condition is the dynamic condition that the (r, r) component of the total stress tensor must be zero. The two latter conditions imply that the dynamic influence from an ambient medium is disregarded. The three boundary conditions, which are to be evaluated at $r = 1$, read

$$u_r = \frac{\partial \eta}{\partial t} \tag{27}$$

$$\tau_{rz} = 0 \tag{28}$$

$$-p + Oh_0\tau_{rr} - \left(\eta + \frac{\partial^2 \eta}{\partial z^2}\right) = 0 \tag{29}$$

The term in the last equation depending on the deformation η represents the linearised jet surface curvature. Furthermore, the initial conditions are

$$\eta(0, z) = \cos kz \quad \text{and} \quad \frac{\partial \eta}{\partial t}(0, z) = 0 \tag{30}$$

indicating that the jet is initially deformed from the cylindrical shape according to a cosine function, and that the surface is initially at rest.

These equations describe the linear problem. They exhibit solutions which are well known from the literature (Goldin et al. 1969; Brenn et al. 2000). For finding the solutions of the equations of motion, we first solve the RCE. All the flow field variables depend on time as per the exponential function $\exp(-\alpha t)$. The quantity α in the exponent of this function is a complex angular frequency which may reduce to a growth or damping rate of the jet surface deformation in aperiodic cases. Given this time dependency, we find for the extra-stress tensor, the solution

$$\tau = 2\frac{1 - De_2\alpha}{1 - De_1\alpha} D =: 2\beta D \tag{31}$$

This means that the extra-stress tensor of the linear viscoelastic fluid differs from the form for a Newtonian material just by a frequency-dependent factor β in front of the rate-of-deformation tensor. This fluid is, therefore, formally identical to a Newtonian one, so that all the results obtained for Newtonian liquids may be transcribed immediately to the present linear viscoelastic case, just with the Ohnesorge number Oh of the Newtonian case replaced by $Oh_v := \beta Oh_0$. The velocity field in the jet due to the deformation reads

$$u_r = \hat{\eta} Oh_v \left[\left(l_v^2 + k^2\right) \frac{I_1(kr)}{I_1(k)} - 2k^2 \frac{I_1(l_v r)}{I_1(l_v)} \right] \exp\left(ikz - \alpha t\right) \tag{32}$$

$$u_z = i\hat{\eta} Oh_v \left[\left(l_v^2 + k^2\right) \frac{I_0(kr)}{I_1(k)} - 2kl_v \frac{I_0(l_v r)}{I_1(l_v)} \right] \exp\left(ikz - \alpha t\right) \tag{33}$$

where $l_v^2 = k^2 - \alpha / Oh_v$ defines a modified wave number and $\hat{\eta}$ is the deformation amplitude. In all complex solutions of the real differential equations, we mean the real parts of the solutions only. For the pressure field, we obtain

$$p = \hat{\eta} \frac{\alpha}{k} \left(2k^2 Oh_v - \alpha\right) \frac{I_0(kr)}{I_1(k)} \exp\left(ikz - \alpha t\right) \tag{34}$$

The dispersion relation of the jet is found by introducing the velocity and pressure fields in the jet into the dynamic zero normal stress boundary condition (29). The result is the well-known relation

$$\alpha^2 - 2\alpha k^2 Oh_v \left[1 - \frac{1}{k} \frac{I_1(k)}{I_0(k)} - \frac{2kl_v}{l_v^2 + k^2} \frac{I_1(k)}{I_0(k)} \left(\frac{I_0(l_v)}{I_1(l_v)} - \frac{1}{l_v} \right) \right] = \tag{35}$$

$$= k\left(1 - k^2\right) \frac{I_1(k)}{I_0(k)} \frac{l_v^2 - k^2}{l_v^2 + k^2}$$

which was first presented by Goldin et al. (1969) and for the Newtonian liquid by Rayleigh (1892). For zero liquid viscosity ($Oh_v \to 0$), this relation reduces to the Rayleigh (1878) result for the inviscid jet in a vacuum.

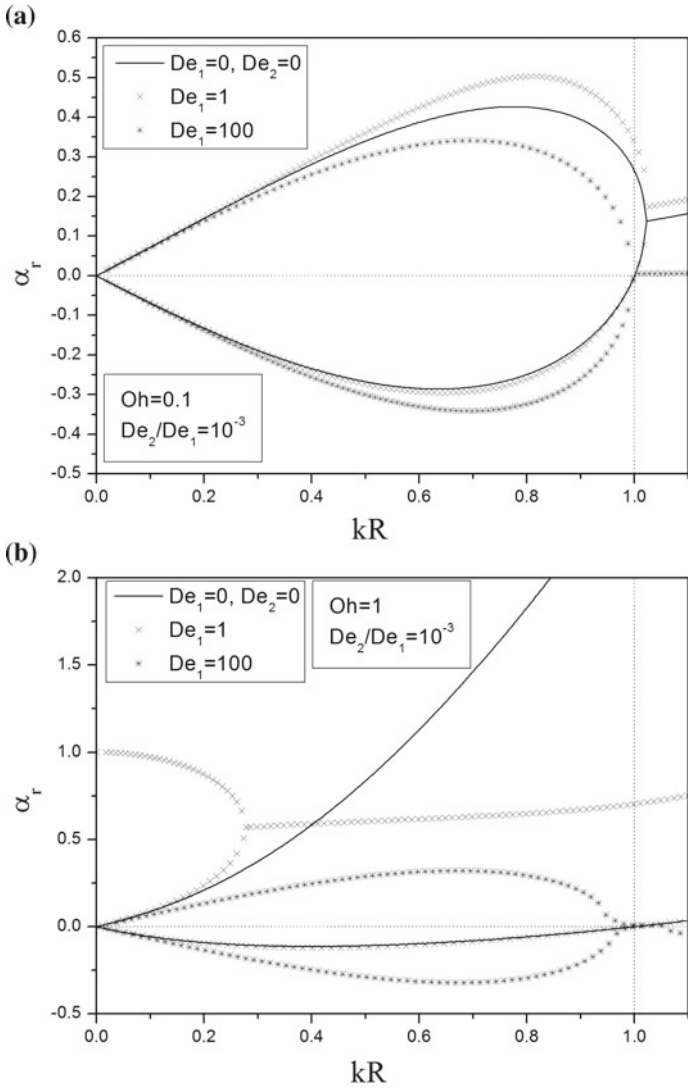

Fig. 31 Dispersion relations of Newtonian and linear viscoelastic jets for varying De_1 at **a** $Oh = 0.1$ and **b** $Oh = 1$. The ratio $De_2/De_1 = 10^{-3}$ is kept constant

The dispersion relation (35) emerging from the linear stability analysis is depicted in Fig. 31 for viscoelastic jets together with the corresponding curves for the Newtonian jet with the same value of Oh. For the ratio De_2/De_1, we set the value of 10^{-3}, corresponding to findings by Brenn and Plohl (2015). This value deviates by several orders of magnitude from the ones often used in the literature. It was found to be the correct value following from oscillating drop experiments for measuring the deformation retardation time.

For disturbance wave numbers $0 \leq k \leq 1$ and for Newtonian fluid, the relation has two real solutions, one positive and one negative. Due to the formulation of the time dependency by the exponential function with a minus sign in front of the exponent αt, the unstable behaviour of the jet is associated with the negative value. For wave numbers $k > 1$, the relation has two complex conjugate solutions with a positive real part. The two values of α represent two waves on the jet surface travelling in different directions and with different phase velocities. In contrast to this, for the linear viscoelastic fluid, the structure of the solutions may be different. At the smaller Oh in Fig. 31a, we find two real solutions with different signs for the viscoelastic case as well as for the Newtonian. At the higher Oh in Fig. 31b, however, the real solutions are replaced by complex ones at $k \geq 0.28$ already. This is an important finding for the viscoelastic jet stability behaviour.

It is seen in Fig. 31 that, at a given Oh, for both De_1 depicted, the viscoelastic jets exhibit larger growth rates of disturbances than their Newtonian counterparts. This would mean that we expect the viscoelastic jet to break up more rapidly than a corresponding Newtonian jet, which is in clear contradiction to the experimental observation showing beads-on-a-string structures with filaments of long lifetime. This discrepancy can be explained by the nonlinear nature of the formation of the latter structure. A description of the dynamics of that phenomenon, therefore, requires a nonlinear stability analysis with account for the strain-hardening behaviour of the liquids.

Linear stability analysis of a sheet The corresponding analysis for a plane liquid sheet is analogous to the analysis for the jet. The geometry of a sheet, however, suggests formulation of the equations of motion in Cartesian coordinates. Furthermore, in the description of the sheet surface deformation, the possibility of the formation of two different shapes of the sheet surface must be accounted for: the deformation may be sinuous or varicose, depending on the relative phases of the wave-like deformations of the two surfaces. The sinuous case is sketched in Fig. 32. We look at this deformation only, since in terms of the order of magnitude of disturbance growth, it is the more 'dangerous' case for the sheet. The resulting dispersion relation for the sinuous sheet deformation reads

$$Oh_{vs}^2 \left[\left(l^2 + k^2\right)^2 \tanh k - 4k^3 l \tanh l \right] + \alpha^2 \frac{\rho_g}{\rho} + k^3 = 0 \tag{36}$$

where the Ohnesorge number for the viscoelastic sheet

$$Oh_{vs} = \frac{\mu_0}{(\sigma H \rho)^{1/2}} \frac{1 - (\alpha - ikU_0)\lambda_2}{1 - (\alpha - ikU_0)\lambda_1} \tag{37}$$

and, in contrast to the jet, the length scale for non-dimensionalisation is the half thickness H of the sheet and ρ_g is the density of the gas ambient to the liquid sheet. The dispersion relation is depicted for five different combinations of Ohnesorge, Deborah and gas Weber number in Fig. 33. It is seen that high Deborah and Weber numbers enhance the sheet instability. Comparing the disturbance growth rates predicted

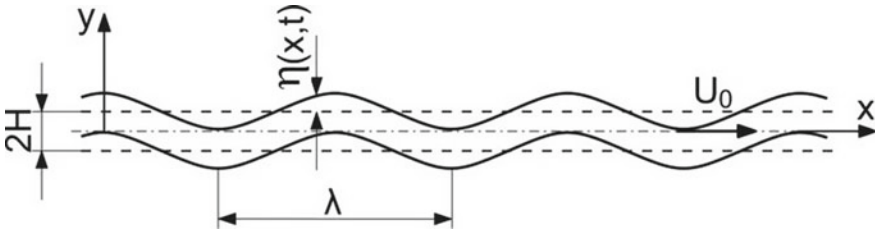

Fig. 32 Surface of a plane liquid sheet with sinuous deformation of wavelength λ

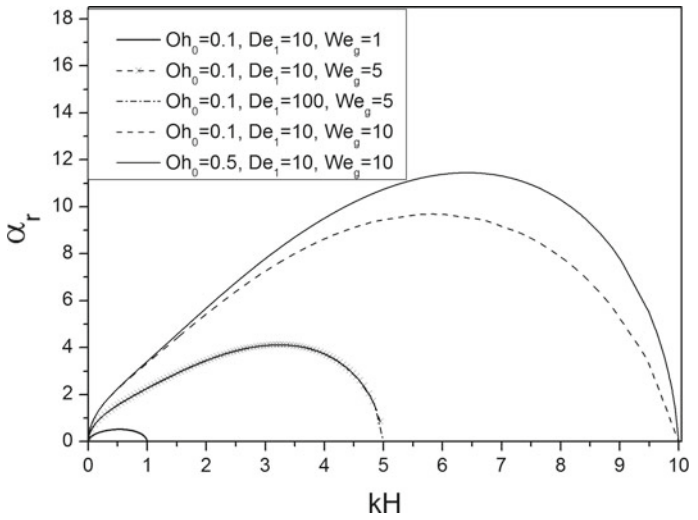

Fig. 33 Dispersion relation of linear viscoelastic sheets for sinuous surface deformation. The ratio $De_2/De_1 = 10^{-3}$

by these data, it is seen that, corresponding to the Kelvin–Helmholtz instability mechanism, the gas Weber number has the strongest influence on the destabilisation of the sheet. While for a given set of parameters, the increase of De_1 by one order of magnitude has a very small influence only, and increasing the gas Weber number from 1 to 5 destabilises the sheet significantly.

In the following section, we discuss experimental studies on the breakup of liquid jets.

4.3 Experimental Studies on Jet Breakup

Experiments on the breakup of laminar jets show marked differences between Newtonian and viscoelastic liquids: while Newtonian jets exhibit the well-known behaviour of spatial and/or temporal growth of surface deformation amplitudes until drops pinch

off, viscoelastic, in particular, strain-hardening liquids form the so-called 'beads-on-a-string' structure, exhibiting drops connected by fine filaments which can live very long and retard the pinch-off of drops.

In drop formation by viscoelastic liquid jet breakup, the importance of stress relaxation in the liquid jet and its timescale were quantified in the literature. As mentioned in Sect. 4.1, Christanti and Walker (2001) investigated the breakup of laminar liquid jets into drops via the beads-on-a-string structure, using solutions of poly(ethylene oxide) (PEO) of varying molecular weight in different mixtures of glycerol and water. The solutions were designed to keep the dynamic viscosity of 5 mPa·s throughout. Drop sizes were measured by image analysis. The drop size spectra measured exhibit bimodal shapes, as depicted in Fig. 34. The size spectrum for the solutions of low molecular PEO exhibits peaks at the size predicted by Rayleigh's inviscid, linear stability analysis (Rayleigh 1878) (the main drops), and at a size smaller by a factor 3 than the main drops (satellite droplets) in agreement with the computational results for inviscid liquid by Bousfield et al. (1986). Given the small Ohnesorge number $O(10^{-2})$ of the jets in these experiments, the good match of the experimental findings with inviscid analytical and computational results is not surprising. The experiments with higher molecular weight of the dissolved polymer in Fig. 34b, however, show that the peak at the smaller size in the drop size spectrum may be suppressed if, at the polymer concentrations at hand, the molecular weight exceeds a value around 10^3kDa. This finding is explained by the stress relaxation time λ_1 of the liquid, which increases with the molecular weight of the polymer in a given solvent. The values of λ_1 of the test liquids presented by Christanti and Walker (2002) are derived from the Zimm model and the Flory–Fox equation and accurate enough to relate their non-dimensional equivalent, the Deborah number $De_1 = \lambda_1(8\sigma/\rho d^3)^{1/2}$, to the suppressed satellite droplet formation. The result is that, for $De_1 \gg 1$, satellite droplets are suppressed (Christanti and Walker 2002).

For the reason of this phenomenon, the related jet breakup length is difficult to predict. An experimental study by Stelter (2001) showed that the relation found by Kroesser and Middleman (1969) may be generalised by forming the Ohnesorge number with an elongational viscosity. The scaling behaviour of this quantity is derived from the elongational characterisation of the liquid.

4.4 Rheological Characterisation of Viscoelastic Liquids

For the evaluation of deformation and breakup models for liquid jets and sheets for spray formation, viscoelastic liquids must be characterised rheologically so as to account for their viscous and elastic behaviour. In many applications, the polymer content is low, so that the shear viscosity does not appreciably deviate from the viscosity of the solvent. The elongational viscosity caused by the deformation of the polymer macromolecules in the solvent, however, may nonetheless be substantially higher than the Trouton viscosity of the Newtonian solvent in uniaxial elongational flow, which is three times the shear viscosity.

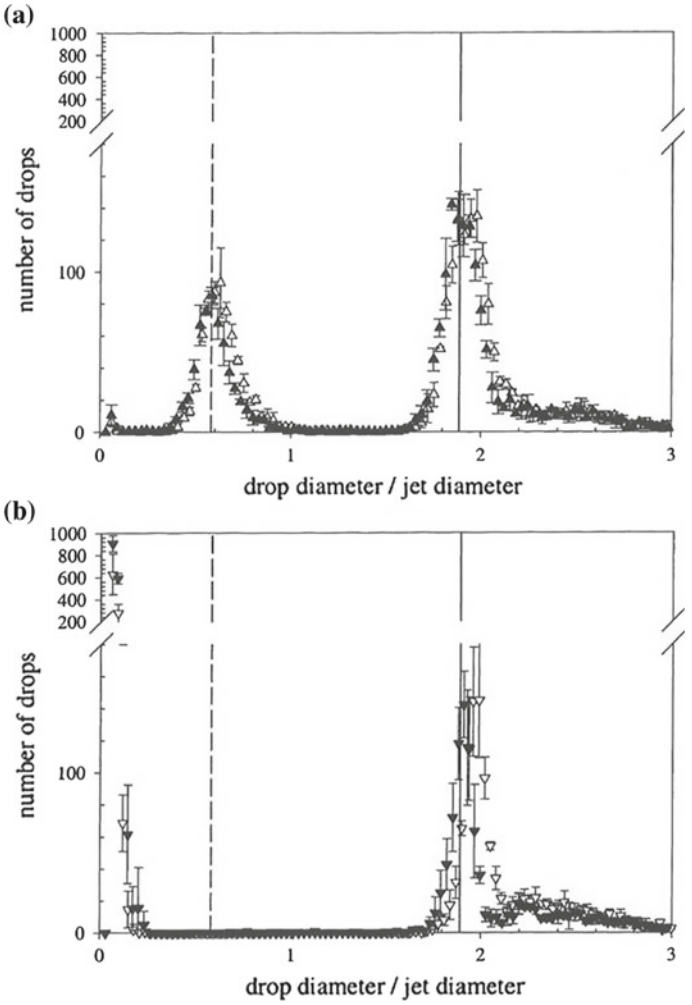

Fig. 34 Drop size spectra measured by image processing in viscoelastic jet breakup (Christanti and Walker 2001). **a**—100 kDa PEO at 0.3%wt. (open triangles) and 1%wt. (filled triangles); **b**—1000 kDa PEO at 0.05%wt (open triangles down) and 0.14%wt. (filled triangles down). Reprinted from Christanti and Walker (2001) with permission from Elsevier

Complex fluids with a polymeric dissolved component at an appreciable concentration may exhibit shear-thinning behaviour, i.e. their shear viscosity decreases with increasing shear rate. This material property is measured in the steady flow of a shear rheometer. Furthermore, viscoelastic liquids exhibit a viscosity which is formulated as a complex conjugate quantity $\mu^* = \mu' - i\mu''$, where the real part corresponds to a viscosity, and the imaginary part to an elasticity. This material property relates an extra stress to a rate of deformation. An alternative for describing

the viscoelastic behaviour of a material at small deformations is to relate the extra stress to a deformation. The material property in this relation is a complex modulus $G^* = G' + iG''$, where G' is the storage and G'' is the loss modulus. The former quantifies elasticity and the latter the viscous loss. Consequently, in a deformation varying harmonically with time at the angular frequency α, complex viscosity and modulus are related as per $G^* = i\alpha\mu^*$. Comparing the real and imaginary parts of the two quantities G^* and μ^*, the storage modulus is related to the imaginary viscosity (the elasticity) as per $G' = \alpha\mu''$ and the loss modulus is $G'' = \alpha\mu'$.

Sufficiently elastic liquids may be characterised by analysing liquid filaments in a filament-stretching elongational rheometer, now termed as the CaBER-type instrument. This device forms a filament between two plates by a step-strain process and measures the thinning of the filament with time. The drainage flow in the filament flow corresponds closely to the actual filament thinning flow in liquid jet and sheet breakup, so that liquid characterisation on the basis of this process is appropriate for spray formation modelling and produces liquid properties relevant to atomisation.

The thinning of the filament is predicted theoretically. Assuming that inertia and body forces are unimportant in this flow, the balance equations of mass and of momentum in the direction of the symmetry (z) axis of the filament are integrated over the filament cross section to obtain a quasi-one-dimensional description of the slender system at hand. The rheological constitutive equation (RCE) of the viscoelastic liquid for formulating the axial normal extra stress is taken from a micro-rheological approach (Yarin 1993). The result is the set of equations

$$\frac{\partial a^2}{\partial t} + \frac{\partial V a^2}{\partial z} = 0 \tag{38}$$

$$0 = \frac{\partial}{\partial z}\left\{\sigma_{zz} a^2 + 2\sigma a\left[1 + \left(\frac{\partial a}{\partial z}\right)^2\right]^{-1/2}\right\} \tag{39}$$

where a is the filament radius and V is the axial velocity component. In viscoelastic liquid filaments, the axial normal stress

$$\sigma_{zz} = \sigma/a \tag{40}$$

is of the order of the stress imposed by the capillary pressure. The axial normal stress is composed of a capillary and a polymeric contribution. Using a microscopic material model relying on macromolecular deformations, we may write

$$\sigma_{zz} = -\sigma/a + ckA_{zz} \tag{41}$$

where c is the concentration of the polymer molecules in the solution, k is the elastic constant of the coiled molecules in the solution and A_{zz} is the zz-component of the orientation–deformation tensor (Stelter et al. 2000; Yarin 1993). The stress is, therefore, related to the deformation of the polymer molecules in the solution. In

the present uniaxial stretching flow, the deformation is dominated by the tensor component A_{zz}, which in the material model is governed by the equation

$$\frac{dA_{zz}}{dt} = 2A_{zz}\frac{\partial V}{\partial z} - \frac{A_{zz}}{\lambda_1} \tag{42}$$

From Eqs. (40) and (41), it follows that $A_{zz} = 2\sigma/cka$. Substituting this result into (42), we obtain the differential equation

$$\frac{d}{dt}\left(\frac{1}{a}\right) = -\frac{4}{a^2}\frac{da}{dt} - \frac{1}{a\lambda_1} \tag{43}$$

for the filament radius $a(t)$. The solution representing the evolution of the diameter $d(t) = 2a(t)$ of a viscoelastic filament with time reads

$$d(t) = d_0 \exp\left(-t/3\lambda_1\right) \tag{44}$$

The analogous analysis for the Newtonian fluid is based on the composition of the stress σ_{zz} in a Newtonian filament

$$\sigma_{zz} = -\frac{\sigma}{a} + 3\mu\frac{\partial V}{\partial z} \tag{45}$$

from the capillary pressure σ/a and the viscous normal stress governed by the Trouton viscosity 3μ. Assuming that this stress is zero in a Newtonian filament (Stelter et al. 2000; Entov and Hinch 1997), the differential equation for the Newtonian filament diameter emerging from Eq. (45) has the solution

$$d_N(t) = d_0 - \frac{\sigma}{3\mu}\,t \tag{46}$$

This equation, however, bases on the assumption that the filament diameter does not depend on the z-coordinate. It therefore predicts the wrong filament diameter evolution if the filament is not cylindrical. An image like Fig. 35 shows that this may be the case in a viscous, Newtonian liquid filament (Stelter 2001). For this case, Papageorgiou (1995) developed a self-similar description of the jet surface shape, from which he derived the corrected filament diameter evolution with time

$$d_{N,P}(t) = d_0 - 0.4254\frac{\sigma}{3\mu}\,t \tag{47}$$

The filament diameter evolution reveals the straining rate

$$\dot{\epsilon} \equiv \frac{\partial V}{\partial z} = -\frac{2}{a}\frac{da}{dt} \tag{48}$$

Fig. 35 Filament of the Newtonian silicon oil Wacker W1000 ($\sigma = 21.2$ mN/m, $\mu = 970$ mPas) in a CaBER-type filament-stretching elongational rheometer (Stelter 2001)

The elongational viscosity in uniaxial straining flow follows from the relation

$$\sigma_{zz} = \mu_{el}\dot{\epsilon} \tag{49}$$

For the viscoelastic liquid, the viscoelastic elongational viscosity is

$$\mu_{el}(t) = \frac{3\sigma\lambda_1}{d_0}\exp\left(t/3\lambda_1\right) \tag{50}$$

while for the Newtonian fluid in uniaxial elongational flow, the elongational viscosity is certainly the Trouton viscosity

$$\mu_{el,N} = 3\mu \tag{51}$$

The corresponding strain rate in the viscoelastic case is obtained as

$$\dot{\varepsilon} = \frac{2}{3\lambda_1} \tag{52}$$

and in the Newtonian case

$$\dot{\varepsilon}_N(t) = \frac{2\sigma}{3\mu d(t)} \tag{53}$$

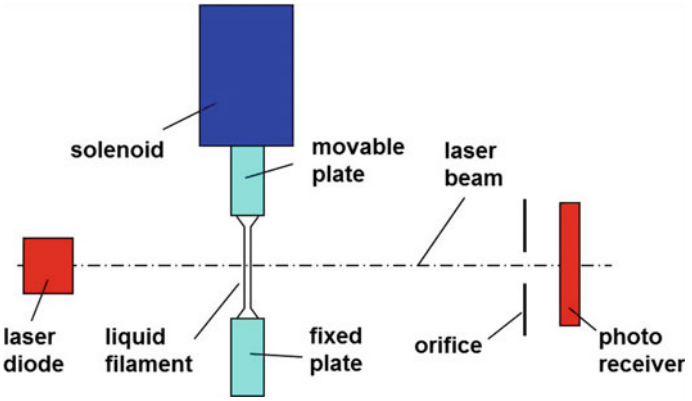

Fig. 36 Setup of an elongational rheometer of the CaBER type (Stelter et al. 2002b)

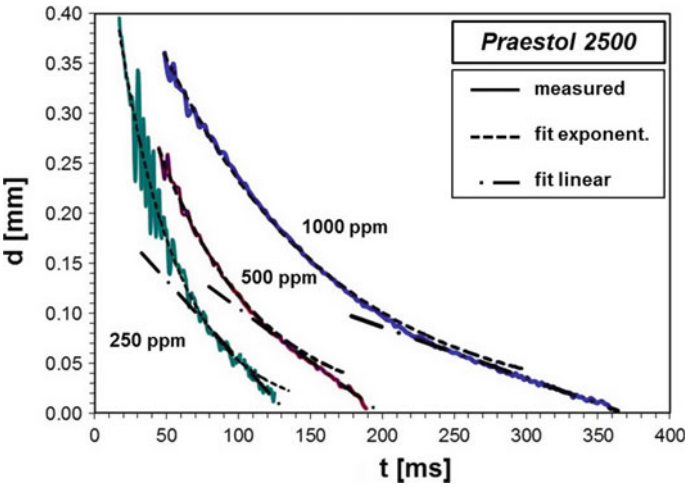

Fig. 37 Data $d(t)$ from the elongational rheometer in Fig. 36 for aqueous Praestol 2500 solutions of three different polymer concentrations (Stelter 2001)

It is interesting to note that, in contrast to the Newtonian liquid, the strain rate of the viscoelastic liquid does not depend on time. The Deborah number $De_1 = \lambda_1 \dot{\varepsilon}$, therefore, exhibits the constant value of $2/3$, which is in favour of a comparability of results from various experiments with this technique.

The experimental realisation of this characterisation technique yields a device as presented by Stelter et al. (2002b) and sketched in Fig. 36. Measurements of the filament diameter as a function of time with aqueous various polymer solutions, such as shown in Fig. 37, showed that the viscoelastic filament thinning does not follow the predicted exponential law throughout its lifetime, but changes its behaviour before pinching. The reason is that the stretching of the polymer macromolecules in the

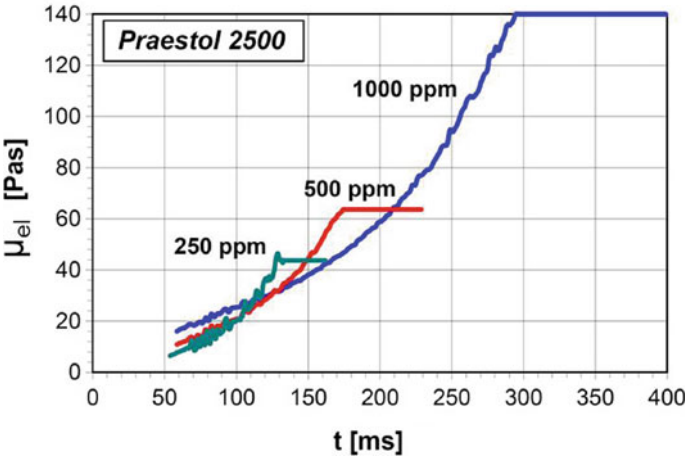

Fig. 38 Elongational viscosity of the filaments shown in Fig. 37 for aqueous Praestol 2500 solutions of three different polymer concentrations (Stelter 2001)

solutions is limited by a maximum achievable molecular deformation (Yarin 1990). From the instant on when this state of maximum deformation is reached, the liquid behaves no longer as elastic, but as a Newtonian fluid with a very high elongational viscosity termed as the 'steady terminal elongational viscosity' (STEV), as shown in Fig. 38. These curves correspond to the data shown in Fig. 10 of Tirtaatmadja and Sridhar (1993), which also show an increase of the elongational viscosity with time and a limitation of the increase by a terminal value. At this state, the thinning of the filament turns from exponential to linear, i.e. the liquid dynamic response upon deformation turns from fully elastic to viscous, Newtonian. This is seen clearly in the measurement data in Fig. 37. In the thinning of liquid filaments in the course of a ligament-mediated spraying process, this same process occurs, so that we may assume that drop formation is dominated by this terminal viscosity.

A systematic study of the steady terminal elongational viscosity (STEV) of solutions of flexible and rigid, rod-like polymers in various solvents was carried out by Stelter et al. (2002a). It was seen that, for a given polymer in its solvent, the value of this material property increases with the polymer concentration. The same trend is seen for the stress relaxation time λ_1. It is an evident option now to depict the former material property of the solutions as a function of the latter in a diagram. This diagram is shown in Fig. 39. In this study, the mass fraction of Praestol 2500 in water, in ethylene glycol and in a methanol–water mixture varied between 62.5 and 500 ppm, and in two different glycerol–water mixtures between 50 and 500 ppm. The mass fractions of poly(ethylene oxide) (PEO) in water were 25 and 50 ppm, and of the copolymer of carboxy-methylcellulose with poly(acrylamide) varied between 1000 and 4000 ppm. For the hydrolysed Praestol 2540 and two poly(acrylamides) named Sedipur (BASF), the mass fraction in water varied between 31.25 and 500 ppm, and for xanthan gum between 1000 and 4000 ppm (Stelter et al. 2002a). The STEV of

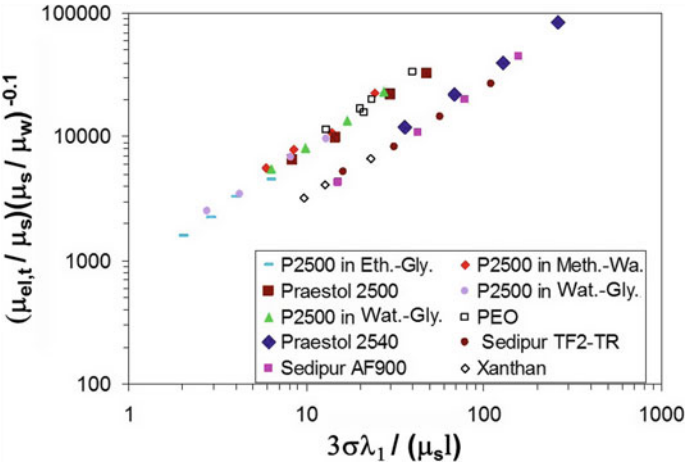

Fig. 39 Non-dimensional steady terminal elongational viscosity of solutions of polymers in various solvents. The data collapse into two groups, one for the flexible and another for the rigid, rod-like polymers (Stelter et al. 2002a)

PEO solutions at higher concentrations could not be measured due to the formation of beads-on-a-string structures which prevent the measurement of the filament thinning in the late stages of the draining. It is interesting to note that there exists a dependency of the steady terminal elongational viscosity on the stress relaxation time of the liquid. One other finding is that the flexible and the rigid, rod-like polymers behave differently in the stretching process of filament thinning. All the data group along two different lines in the diagram, where the upper line is formed by the flexible and the lower one by the rigid, rod-like polymers. The two terminal elongational viscosities for the aqueous solutions are given as functions of the stress relaxation time by the equations

$$\mu_{el,t,flex} = 3074.9\lambda_1 + 0.003 \tag{54}$$

$$\mu_{el,t,rigid} = 1288.1\lambda_1 + 0.003 \tag{55}$$

where the elongational viscosities are obtained in Pa·s if the stress relaxation time is entered in s (Stelter et al. 2002b). The ratio of the factors in front of λ_1 flexible to rigid exhibits the value of 2.39. This empirical value will gain big importance for the characterisation of spray formation processes from solutions of flexible or rigid, rod-like polymers in water, as will be pointed out later.

Forming non-dimensional numbers with this viscosity to characterise drop formation may be a promising approach to a universal description of ligament-mediated drop formation from Newtonian and viscoelastic liquids.

4.5 Non-Newtonian Sprays

For the design of sprays, the description of their formation should include a prediction of the drop size appropriate for the application, either in a spectral, local or in an integral, global manner. Due to the complicated liquid breakup and flow processes producing the spray drops, the most promising approach is to formulate a normalised mean drop size of the spray as a function of a product of powers of non-dimensional numbers relevant to the process. The correct representation, i.e. the correct set of non-dimensional numbers, follows from a dimensional analysis and turns out to be, e.g., of the form $D_{32}/d = f(Re_{el}, We)$. In this function, the Reynolds number Re_{el} formulated with an equivalent elongational viscosity turns out crucial for a universal representation of the formation of sprays from Newtonian and non-Newtonian viscoelastic liquids.

Mechanical degradation of polymers in strong flows Molecular properties of macromolecular compounds may be subject to changes under strong mechanical loads. Strong straining and shearing flows tend to deform the macromolecules of (flexible) polymeric substances and to turn the molecules of rigid, rod-like polymers. Flexible macromolecules are uncoiled and stretched in straining and shearing flows (de Gennes 1974). The mechanical strength of the molecules is limited. Strong straining and shearing flows may, therefore, lead to mechanical degradation of the polymer in the solution, breaking the macromolecules into smaller pieces. This reduction of the molecular weight of the polymer changes the stress relaxation time. Since this material property is important in the modelling of the rheological material behaviour of the polymer solutions, the potential of the flows through the atomisers for breaking the macromolecules was investigated. Varying the flow rate through various flat-fan atomisers, the strain and shear rates in the nozzle flow were varied (Stelter et al. 2002b). Liquid samples were taken from the sprays and allowed to rest long enough so that foam and air bubbles in the liquid disappeared. Measuring the liquid stress relaxation time of these sprayed liquid samples revealed values which were systematically less than the relaxation times of the fresh solutions. The results for aqueous solutions of four different polymers at varying mass fraction are shown in Fig. 40, where λ_1 and $\lambda_{1,0}$ are the stress relaxation times of the sprayed and of the fresh solution, respectively. The independent variable

$$De^* = \lambda_{1,0} \frac{U}{d_e} \frac{d_{\min}}{d_{\max}} \tag{56}$$

is a modified convective Deborah number accounting for the contraction of the cross section in the atomiser and for the flow rate through the nozzle. The diameters characterising the bore geometries of the flat-fan atomisers used in the present study are listed in Table 1. The fact that the time elapsed between the spraying of the test liquids and the measurements of the relaxation time indicates that the molecular process reducing the relaxation time led to a permanent change of the molecular properties of the dissolved polymer. This is seen in contrast to the (reversible) break

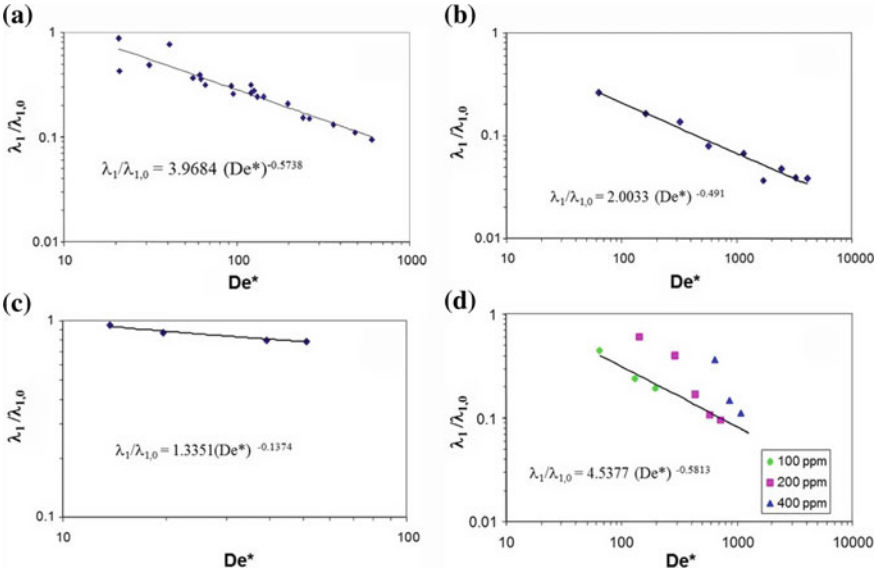

Fig. 40 Decrease of the stress relaxation time λ_1 against the values of the fresh solution due to mechanical degradation of the polymers in the nozzle flow. Aqueous solutions of **a**—Praestol 2500 at 200 ppm wt., **b**—PEO at 100 ppm wt., **c**—CMC-g-PAM at 1500 ppm wt., **d**—Praestol 2540 at the mass fractions in the legend (Stelter et al. 2002b)

down of micelles in micellar solutions by straining or shearing. The micelles are re-established after some time when the solution is kept at rest. This is not the case in the present polymer solutions.

Sprays from flat-fan sheet breakup Pressure atomisers of the flat-fan type are used in many fields, among them for pesticide spraying in agriculture. The shape of the bore in the atomiser produces a flat-fan liquid sheet at the atomiser exit. The sheet is Kelvin–Helmholtz unstable and develops waves on its surface, which are unstable and break the sheet into ligaments. The ligaments finally break down into the spray drops (Dombrowski and Johns 1963). Spray formation by flat-fan pressure atomisers is, therefore, ligament mediated and belongs to the group of processes we presently discuss.

Figure 41 shows a flat-fan sheet of a 100 ppm wt. aqueous poly(acrylamide) solution Praestol 2500 produced by an atomiser Lechler 632.304 at the flow rate of 40 l/h. The zoom-in photograph shows beads-on-a-string structured ligaments and drops which clearly indicates the importance of the ligament-thinning process found in the rheometric characterisation above in the formation of drops. The approach to represent drop formation by properties of the ligament in its late stages of thinning, in particular, by its steady terminal elongational viscosity, is therefore promising. For developing this universal characterisation of the atomisation result, series of drop size measurements in flat-fan sprays were carried out with a phase-Doppler

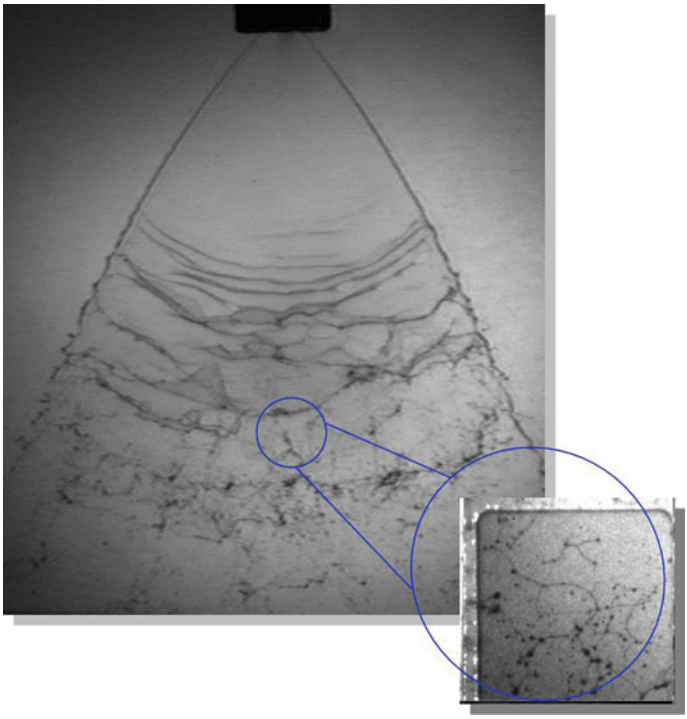

Fig. 41 Flat-fan-shaped sheet of a 100 ppm wt. aqueous Praestol 2500 solution from the flat-fan atomiser Lechler 632.304 (Stelter 2001). The zoom-in shows that the sheet breakup goes along with the formation of beads-on-a-string structures originating from ligament thinning

anemometer (PDA) by Stelter et al. (2002b). The measurements were carried out in a spray region close to the breakup zone so as to characterise the primary atomisation result without influence from drop–drop interactions and evaporation. Global mean drop sizes are derived from the measured local drop sizes, weighted by the local spray cross-sectional areas and the local drop number fluxes. In this manner, the global mean Sauter-mean drop size of a spray characterised by phase-Doppler measurements may be deduced from the local measurement data as per

$$D_{32} = \frac{\sum_{j=1}^{J} \sum_{i=1}^{I} d_{i,j}^3 \dot{n}_{i,j} \Delta A_j}{\sum_{j=1}^{J} \sum_{i=1}^{I} d_{i,j}^2 \dot{n}_{i,j} \Delta A_j} \tag{57}$$

In this equation, $d_{i,j}$ is the drop size and $\dot{n}_{i,j}$ is the number flux of drops of size class i detected at position j in the spray and ΔA_j is the partial area of the spray cross section represented by the local measurements at position j.

Table 1 Properties of flat-fan atomisers and test liquids in the experiments of Fig. 42

#	Nozzle type	d_e [mm]	$d_{\min}$ [mm]	$d_{\max}$ [mm]	Flow rates [l/h]	Polymer mass fraction [ppm]
1	Spraying systems TEEJET 80015	0.76	0.5	1.16	20–55	0–400 P2500, P2540
2	Spraying systems TEEJET 80015	0.74	0.4	1.16	30–50	0
3	Lechler 632.301	0.7	0.52	0.93	30–41	0–400 P2500

Table 1 lists the geometrical properties of the three flat-fan atomisers used in the study, together with the flow rates covered by these experiments and the polymers with the range of their mass fractions in the aqueous solutions.

In physical processes as complicated as spray formation, dimensional analysis is a way to find a universal representation of the dependencies of the process result on the various influencing parameters. For a dimensional analysis of the atomisation process, we start from the list of relevant parameters, which is the global mean Sauter-mean drop diameter D_{32}, a length scale d of the atomiser, for which we take the area-equivalent orifice diameter, the volume flow rate-equivalent liquid velocity U as well as the liquid properties σ, ρ and $\mu_{el,eff}$, where the latter is an effective elongational viscosity which we formulate as $De_d k\sigma\lambda_1/d$, with the convective Deborah number $De_d = \lambda_1 U/d$ and the empirical factor k allowing for the representation of the spray property at hand. Given the three basic dimensions involved in the problem, this list of six relevant parameters results in three non-dimensional numbers characterising the spray formation process, which are $Re_{el}{=}U d\rho/\mu_{el,eff}$, $We{=}U^2 d\rho/\sigma$ and D_{32}/d. We therefore seek to represent the normalised global mean Sauter-mean diameter of the spray drops as a function $D_{32}/d{=}f\,(Re_{el},\, We)$ (Stelter et al. 2002b).

In doing so, we start from the representation of the normalised D_{32} of pure solvent, i.e. water sprays, by a function $D_{32}/d = C\,Re_{el}^m We^n$. Fitting the function to the experimental data means determining the parameters C, m and n. The next step is to fit the data for the solutions of flexible polymers in water to those of the water sprays by appropriately selecting the empirical factor k, while keeping C, m and n constant. We arrive at a universal representation of these two groups of sprays by selecting $k = k_{flexible} = 1/1500$. In doing the same for the data from the rigid, rod-like polymers dissolved in water, we find that the empirical factor $k_{flexible}$ must yield a ratio to $k = k_{rigid}$ for these polymers of 2.39, which equals the ratio of $(d\mu_{el,t}/d\lambda_1)_{flexible}/(d\mu_{el,t}/d\lambda_1)_{rigid}$ from the rheometric characterisation. This finding applies to the representation of all the spray properties investigated here. The factor k for the solutions of rigid polymers, therefore, is $k_{rigid} = 1/3581$ (Stelter et al. 2002b).

The diagram in Fig. 42 shows the non-dimensional global Sauter-mean drop size of sprays of water, together with aqueous solutions of flexible and of rigid, rod-like polymers produced by flat-fan atomisers. Given the three different atomiser geometries

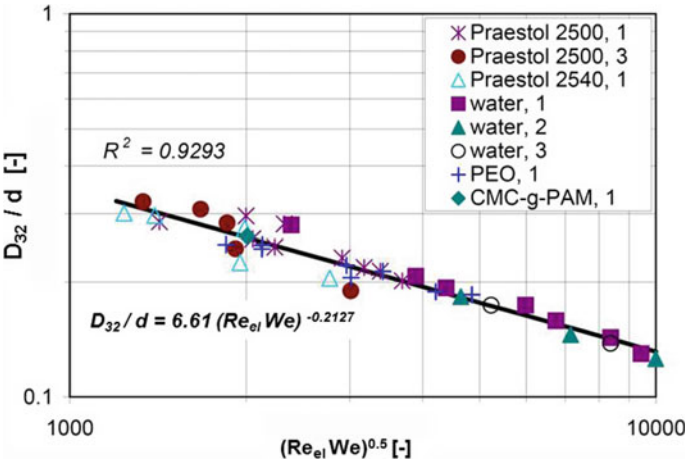

Fig. 42 Normalised global Sauter-mean drop size of water and polymer solution sprays from three different flat-fan atomisers (Stelter et al. 2002b)

and the four different polymers plus the water sprays involved, the universality in the representation of the mean drop size is excellent. This approach is, therefore, promising for a universal representation of drop sizes in sprays of viscoelastic liquids produced by flat-fan pressure atomisers. The data show the expected effect that a decrease of the characteristic number $Re_{el}\ We$ makes the mean Sauter-mean drop size in the flat-fan sprays increase. This is plausible and observed in Newtonian sprays also, where an increase of, e.g., the liquid velocity makes mean spray drop sizes decrease and vice versa. It is interesting to note that, for the viscoelastic sprays, the Reynolds number newly defined with the effective elongational viscosity $\mu_{el,eff}$ turns equivalent to the inverse of a capillary Deborah number squared as per $Re_{el} = 1/(kDe_c^2)$ with $De_c = \lambda_1/(\sigma/\rho d^3)^{1/2}$. The characteristic number determining the global mean Sauter-mean drop size in the flat-fan sprays, therefore, rather corresponds to a ratio We/De_c^2. The convective influence on the sheet breakup is represented by the Weber number, where the thermodynamic state of the ambient air was not varied in the above experiments, so that it does not appear in the analysis, despite its influence through the Kelvin–Helmholtz instability (Stelter et al. 2002b).

In the experimental study discussed here, the above-presented characterisation of sprays from flat-fan atomisers was found to hold for spectral properties of the spray drop ensembles also. The design of liquids to be atomised, e.g., for crop spraying in agriculture, aims to minimise the formation of small drops in the atomisation process, which are transported by wind to undesired places and may harm cultures. The polymeric compounds used for this purpose are called ‘anti-drift agents’. It is, therefore, desirable to predict the influence of polymeric ingredients in the liquid recipes on the drop size spectra. In investigating this potential of the present characterisation method, the data in Fig. 43 were found.

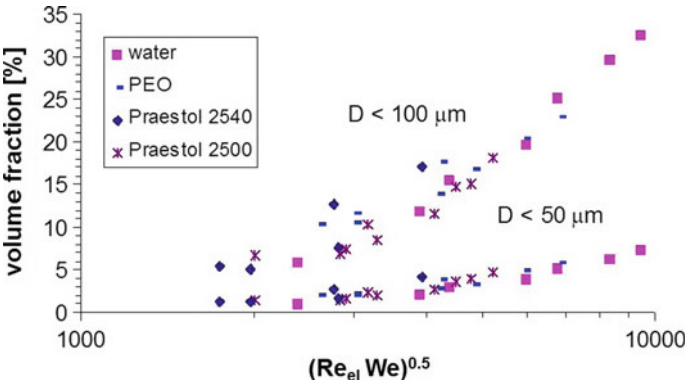

Fig. 43 Volume fractions of drops with sizes less than 100 and 50 µm in the global drop size spectra of various sprays from flat-fan spray atomiser 1 (Stelter et al. 2002b)

Table 2 Properties of pressure-swirl atomisers and test liquids in the experiments of Fig. 44

Atomiser #	Atomiser type	d_e[mm]	Flow rates [l/h]	Polymer mass fraction [ppm]
1	Schlick model 121 V	0.45	6–14	0–100 P2500, PEO
2	Schlick model 121 V	0.72	10–22	0–100 P2500, PEO

Sprays from hollow-cone sheet breakup Pressure atomisers producing sprays of the hollow-cone type, called pressure-swirl atomisers, are used in many applications, among them spray drying and spray painting. The atomiser type stands out for the production of fine droplets at a moderate liquid flow rate. This is due to the formation of a conical liquid sheet at the atomiser exit with an air core. The sheet thins downstream and due to its Kelvin–Helmholtz instability, it develops waves on the surface which grow and break the sheet into ligaments. The ligaments finally break down into the spray drops. The sheet differs geometrically from the flat-fan case in that it is closed in the circumferential direction, thus avoiding the formation of a free rim at a sheet edge since this does not exist. Spray formation by pressure-swirl atomisers is ligament mediated and belongs to the group of processes we presently discuss. A series of experiments with PDA drop size measurements were carried out using various aqueous polymer solutions for this atomiser type also. Table 2 lists the geometrical properties of the two pressure-swirl atomisers used in the study, together with the flow rates covered by these experiments and the polymers with the range of their mass fractions in the aqueous solutions.

The dimensional analysis of the atomisation process by a pressure-swirl atomiser differs from the flat-can case in that the liquid sheet thickness at the atomiser orifice is an additional parameter, which is fixed by the atomiser bore geometry in flat-fan atomisers. This additional parameter is represented by quantifying the ratio of the pressure drop across the atomiser to the kinetic energy (or dynamic pressure)

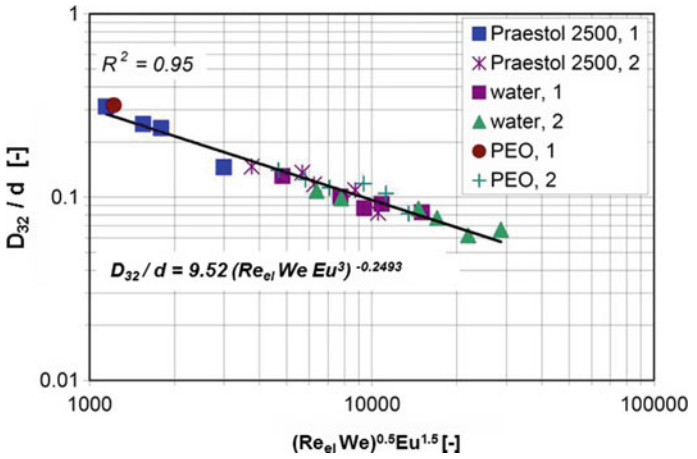

Fig. 44 Normalised global Sauter-mean drop size of water and aqueous polymer solution sprays from two different pressure-swirl atomisers (Stelter et al. 2002b)

of the liquid produced, which is called the Euler number Eu. This number adds to the set of numbers found for flat-fan atomisation. The non-dimensional numbers representing the atomisation process with pressure-swirl atomisers are, therefore, $Re_{el}{=}U\,D\rho/\mu_{el,eff}$, $We{=}U^2 d\rho/\sigma$, $Eu = \Delta p/\rho U^2$ and D_{32}/d. We seek to represent the normalised global Sauter-mean diameter of the spray drops as a function $D_{32}/d = f(Re_{el}, We, Eu)$.

The diagram in Fig. 44 shows the non-dimensional global Sauter-mean drop size of sprays of water and aqueous polymer solutions produced by pressure-swirl atomisers (Stelter et al. 2002b). For spray formation by pressure-swirl atomisers, solutions of flexible polymers were investigated only. Given the two different atomiser geometries and the two different aqueous polymer solutions plus the water sprays involved, the universality in the representation of the mean drop size is excellent. This approach is promising for a universal representation of drop sizes in sprays of viscoelastic liquids produced by pressure atomisers.

4.6 Concluding Remarks

The study on spray formation from viscoelastic liquids presented shows that, for the modelling of spray formation by viscoelastic liquid sheet breakup, an appropriate characterisation of the liquid rheological behaviour upon deformation is needed. For spray formation by pre-filming atomisers, which break down to form the spray drops, mediated by ligaments, the property of particular importance is the behaviour in uniaxial elongational flow. In measurements of the elongational viscosity, it turns out that the ligament lifetime and the final drop size formed by their breakup are determined

by a steady terminal value of the elongational viscosity, which we managed to relate to the stress relaxation time of the liquid. Further research in this field will replace the empiricism of the model presented by fundamental knowledge about the molecular deformation and alignment processes in the filament-stretching flow.

References

Attané P, Girard F, Morin V (2007) An energy balance approach of the dynamics of drop impact on a solid surface. Phys Fluids 19(1):012101

Barnes HA (1995) A review of the slip (wall depletion) of polymer solutions, emulsions and particle suspensions in viscometers: its cause, character, and cure. J Non-Newton Fluid Mech 56(3):221–251

Barnes AC, Neilson GW, Enderby JE (1995) The structure and dynamics of aqueous solutions containing complex molecules. J Mol Liq 65–66:99–106

Bartolo D, Boudaoud A, Narcy G, Bonn D (2007) Dynamics of non-newtonian droplets. Phys Rev Lett 99(17)

Bazilevskii AV, Voronkov SI, Entov VM, Rozhkov AN (1981) On orientational effects at breakup of jets and threads of dilute polymer-solutions. Dokl Akad Nauk SSSR 257(2):336–339

Bechtel SE, Bogy DB, Talke FE (1981) Impact of a liquid drop against a flat surface. IBM J Res Dev 25(6):963–971

Bergeron V, Martin J-Y, Vovelle L (1998) Interaction of droplets with a surface: impact and adhesion. In: Fifth international symposium on adjuvants and agrochemicals memphis, Tennessee, USA, 17–21 Aug 1998

Bergeron V, Bonn D, Martin J-Y, Vovelle L (2000) Controlling droplet deposition with polymer additives. Nature 405:772–775

Bergeron V, Martin J-Y, Vovelle L (2003) Use of polymers as sticking agents. US Pat 6:534–563

Bernardin JD, Mudawar I (2002) A cavity activation and bubble growth model of the leidenfrost point. J Heat Transf 124(5):864–874

Bertola V (2004) Drop impact on a hot surface: effect of a polymer additive. Experiments in fluids 37(5):653–664

Bertola V (2009a) Wicking with a yield stress fluid. J Phys Condens Matter 21(3)

Bertola V (2009b) An experimental study of bouncing leidenfrost drops: comparison between newtonian and viscoelastic liquids. Int J Heat Mass Transf 52(7):1786–1793

Bertola V (2010) Effect of polymer additives on the apparent dynamic contact angle of impacting drops. Colloids Surf A: Physicochem Eng Asp 363(1–3):135–140

Bertola V (2013) Dynamic wetting of dilute polymer solutions: the case of impacting droplets. Adv Colloid Interface Sci 193–194:1–11

Bertola V (2014) Effect of polymer concentration on the dynamics of dilute polymer solution drops impacting on heated surfaces in the leidenfrost regime. Exp Therm Fluid Sci 52:259–269

Bertola V (2015) An impact regime map for water drops impacting on heated surfaces. Int J Heat Mass Transf 85:430–437

Bertola V, Sefiane K (2005) Controlling secondary atomization during drop impact on hot surfaces by polymer additives. Phys Fluids 17(10):108104

Bertola V, Wang M (2015) Dynamic contact angle of dilute polymer solution drops impacting on a hydrophobic surface. Colloids Surf A: Physicochem Eng Asp 481:600–608

Biance A-L, Chevy F, Clanet C, Lagubeau G, Quéré D (2006) On the elasticity of an inertial liquid shock. J Fluid Mech 554(1):47–66
Biolè D, Bertola V (2015a) The fuzzy interface of a drop. Comput Vis Sci 17(1):19–32
Biolè D, Bertola V (2015b) A goniometric mask to measure contact angles from digital images of liquid drops. Colloids Surf A: Physicochem Eng Asp 467:149–156
Biolè D, Bertola V (2015c) The role of the microscale contact line dynamics in the wetting behaviour of complex fluids. Arch Mech 67(5):401–414
Biolè D, Wang M, Bertola V (2016) Assessment of direct image processing methods to measure the apparent contact angle of liquid drops. Exp Therm Fluid Sci 76:296–305
Black K, Bertola V (2013) Non-newtonian leidenfrost drops. At Sprays 23(3):233–247
Bonhoeffer B, Kwade A, Juhnke M (2017) Impact of formulation properties and process parameters on the dispensing and depositioning of drug nanosuspensions using micro-valve technology. J Pharmaceut Sci 106(4):1102–1110
Borodin O, Smith GD (2000) Molecular dynamics simulations of poly(ethylene oxide)/lii melts. 2. dynamic properties. Macromolecules 33(6):2273–2283
Bousfield DW, Keunings R, Marrucci G, Denn MM (1986) Nonlinear analysis of the surface tension driven breakup of viscoelastic filaments. J Non-Newton Fluid Mech 21:79–97
Brandrup J, Immergut EH, Grulke EA, Abe A, Bloch DR (2005) Polymer handbook, 4th edn. Wiley
Brenn G, Plohl G (2015) The oscillating drop method for measuring the deformation retardation time of viscoelastic liquids. J Non-Newton Fluid Mech 223:88–97
Brenn G, Plohl G (2017) The formation of drops from viscoelastic liquid jets and sheets—an overview. At Sprays 27:285–302
Brenn G, Liu ZB, Durst F (2000) Linear analysis of the temporal instability of axisymmetrical non-newtonian liquid jets. Int J Multiph Flow 26:1621–1644
Chandra S, Avedisian CT (1991) On the collision of a droplet with a solid surface. Proc R Soci Lond A: Math Phys Eng Sci 432:13–41
Chandrasekhar S (1961) Hydrodynamic and hydromagnetic stability. International series of monographs on physics. Clarendon Press
Chen L, Wang Y, Peng X, Zhu Q, Zhang K (2018) Impact dynamics of aqueous polymer droplets on superhydrophobic surfaces. Macromolucles 51(19):7817–7827
Chen S, Bertola V (2016a) The impact of viscoplastic drops on a heated surface in the leidenfrost regime. Soft Matter 12:7624–7631
Chen S, Bertola V (2016b) Jumps, somersaults, and symmetry breaking in leidenfrost drops. Phys Rev E 94(2)
Chibowski E (2003) Surface free energy of a solid from contact angle hysteresis. Adv Colloid Interface Sci 103(2):149–172
Chibowski E (2007) On some relations between advancing, receding and Young's contact angles. Adv Colloid Interface Sci 133(1):51–59
Christanti Y, Walker LM (2001) Surface tension driven jet break up of strain-hardening polymer solutions. J Non-Newton Fluid Mech 100:9–26
Christanti Y, Walker LM (2002) Effect of fluid relaxation time of dilute polymer solutions on jet breakup due to a forced disturbance. J Rheol 46:733–748
Clanet C, Béguin C, Richard D, Quéré D (2004) Maximal deformation of an impacting drop. J Fluid Mech 517:199–208
Coussot P, Gaulard F (2005) Gravity flow instability of viscoplastic materials: the ketchup drip. Phys Rev E 72:031409
Crooks R, Cooper-White J, Boger DV (2001) The role of dynamic surface tension and elasticity on the dynamics of drop impact. Chem Eng Sci 56:5575–5592
de Gennes PG (1974) Coil-stretch transition of dilute flexible polymers under ultrahigh velocity gradients. J Chem Phys 60(12):5030–5042
de Gennes PG (1985) Wetting: statics and dynamics. Rev Mod Phys 57(3):827–863
Dexter RW (1996) Measurement of extensional viscosity of polymer solutions and its effects on atomization from a spray nozzle. At Sprays 6:167–191

Dombrowski N, Johns WR (1963) The aerodynamic instability and disintegration of viscous liquid sheets. Chem Eng Sci 18:203–214
Dussan EB (1985) On the ability of drops or bubbles to stick to non-horizontal surfaces of solids. Part 2. small drops or bubbles having contact angles of arbitrary size. J Fluid Mech 151:1–20
Eggers J (1997) Nonlinear dynamics and breakup of free-surface flows. Rev Mod Phys 69:865–930
Eggers J, Fontelos MA, Josserand C, Zaleski S (2010) Drop dynamics after impact on a solid wall: theory and simulations. Phys Fluids 22(6):062101
Entov VM, Hinch EJ (1997) Effect of a spectrum of relaxation times on the capillary thinning of a filament of elastic liquid. J Non-Newton Fluid Mech 72:31–53
Ford RE, Furmidge CGL (1967) Impact and spreading of spray drops on foliar surfaces. Soc Chem Ind Monogr 25:32–417
Fujimoto H, Oku Y, Ogihara T, Takuda H (2010) Hydrodynamics and boiling phenomena of water droplets impinging on hot solid. Int J Multiph Flow 36(8):620–642. ISSN 0301-9322
German G, Bertola V (2009a) Impact of shear-thinning and yield-stress drops on solid substrates. J Phys: Condens Matter 21(37):375111
German G, Bertola V (2009b) Review of drop impact models and validation with high-viscosity newtonian fluids. At Sprays 19(8)
German G, Bertola V (2010a) The free-fall of viscoplastic drops. J Non-Newton Fluid Mech 165(13–14):825–828
German G, Bertola V (2010b) Formation of viscoplastic drops by capillary breakup. Phys Fluids 22(3):033101
Goldin M, Yerushalmi J, Pfeffer R, Shinnar R (1969) Breakup of a laminar capillary jet of a viscoelastic fluid. J Fluid Mech 38:689–711
Gottfried BS, Lee CJ, Bell KJ (1966) The leidenfrost phenomenon: film boiling of liquid droplets on a flat plate. Int J Heat Mass Transf 9(11):1167–1188
Harrison GM, Mun R, Cooper G, Boger DV (1999) A note on the effect of polymer rigidity and concentration on spray atomisation. J Non-Newton Fluid Mech 85:93–104
Hartnett JP, Hu RYZ (1986) Role of rheology in boiling studies of viscoelastic liquids. Int Commun Heat Mass Transf 13(6):627–637. ISSN 0735-1933
Josserand C, Thoroddsen ST (2016) Drop impact on a solid surface. Ann Rev Fluid Mech 48(1):365–391
Kalashnikov VN, Askarov AN (1989) Relaxation time of elastic stresses in liquids with small additions of soluble polymers of high molecular weights. J Eng Phys Thermophys 57(2):874–878
Keshavarz B, Sharma V, Houze EC, Koerner MR, Moore JR, Cotts PM, Threlfall-Holmes P, McKinley GH (2015) Studying the effects of extensional properties on atomization of weakly viscoelastic solutions using rayleigh ohnesorge jetting extensional rheometry (rojer). J Non-Newton Fluid Mech 222:171–189
Kim KY, Kang SL, Kwak H-Y (2004) Bubble nucleation and growth in polymer solutions. Polym Eng Sci 44(10):1890–1899
Kim JH, Shi W-X, Larson RG (2007) Methods of stretching dna molecules using flow fields. Langmuir 23(2):755–764
Kroesser FW, Middleman S (1969) Viscoelastic jet stability. AIChE J 15:383–386
Kroger M (2015) Simple, admissible, and accurate approximants of the inverse langevin and brillouin functions, relevant for strong polymer deformations and flows. J Non-Newton Fluid Mech 223:77–87
Lefebvre A (1988) At Sprays. Combustion (Hemisphere Publishing Corporation). Taylor & Francis. ISBN 9780891166030
Lin SP, Reitz RD (1998) Drop and spray formation from a liquid jet. Ann Rev Fluid Mech 30(1):85–105
Lindner A, Vermant J, Bonn D (2003) How to obtain the elongational viscosity of dilute polymer solutions? Physica A 319:125–133

Lumley JL (1973) Drag reduction in turbulent flow by polymer additives. J Polym Sci: Macromol Rev 7(1):263–290
Luu L-H, Forterre Y (2009) Drop impact of yield-stress fluids. J Fluid Mech 632:301–327
Mao T, Kuhn D, Tran H (1997) Spread and rebound of liquid droplets upon impact on flat surfaces. AIChE J 43(9):2169–2179
Marmottant P, Villermaux E (2004) Fragmentation of stretched liquid ligaments. Phys Fluids 16:2732–2741
Moreira ALN, Moita AS, Panao MR (2010) Advances and challenges in explaining fuel spray impingement: how much of single droplet impact research is useful? Prog Energy Combust Sci 36(5):554–580
Mun RP, Byars JA, Boger DV (1998) The effects of polymer concentration and molecular weight on the breakup of laminar capillary jets. J Non-Newton Fluid Mech 74:285–297
Mun RP, Young BW, Boger DV (1999) Atomisation of dilute polymer solutions in agricultural spray nozzles. J Non-Newton Fluid Mech 83:163–178
Mundo C, Sommerfeld M, Tropea C (1995) Droplet-wall collisions: experimental studies of the deformation and breakup process. Int J Multiph Flow 21(2):151–173
Negri M, Ciezki HK (2015) Effect of elasticity of boger fluids on the atomization behaviour of an impinging jet injector. At Sprays 25:695–714
Nigen S (2005) Experimental investigation of the impact of an apparent yield-stress material. At Sprays 15:103–117
Oliveira MSN, Yeh R, McKinley GH (2006) Iterated stretching, extensional rheology and formation of beads-on-a-string structures in polymer solutions. J Non-Newton Fluid Mech 137(1):137–148. Extensional Flow
Papageorgiou DT (1995) On the breakup of viscous liquid threads. Phys Fluids 7(7):1529–1544
Park GY, Harrison GM (2008) Effects of elasticity on the spraying of a non-newtonian fluid. At Sprays 18:243–271
Pasandideh-Fard M, Qiao YM, Chandra S, Mostaghimi J (1996) Capillary effects during droplet impact on a solid surface. Phys fluids 8(3):650–659
Pedersen CO (1970) An experimental study of the dynamic behavior and heat transfer characteristics of water droplets impinging upon a heated surface. Int J Heat Mass Transf 13(2):369–381. ISSN 0017-9310
Peterlin A (1966) Hydrodynamics of linear macromolecules. Pure Appl Chem 12(1–4):563–586
Plateau J (1867) Lettre au sujet de la transformation spontanée d'un cylindre liquide en sphères isolées. Comptes Rendus des Séances de l'Académie des Sciences 65:290–291
Quéré D (2013) Leidenfrost dynamics. Ann Rev Fluid Mech 45:197–215
Rayleigh L (1878) On the instability of jets. Proc Lond Math Soc 10:4–13
Rayleigh L (1879) On the capillary phenomena of jets. Proc R Soc Lon Ser A Math Phys Sci 29:71–97
Rayleigh L (1892) On the instability of a cylinder of viscous liquid under capillary force. Philos Mag 34:145–154
Rein M (1993) Phenomena of liquid drop impact on solid and liquid surfaces. Fluid Dyn Res 12(2):61–93
Rein M (ed) (2003) Drop-Surface interactions, CISM courses and lectures no. 456. Springer, Wien-New York
Rogers GP, Barnes HA (2001) New measurements of the flow-curves for carbopol dispersions without slip artefacts. Rheologica Acta 40:499–503
Roisman IV (2009) Inertia dominated drop collisions. ii. An analytical solution of the navierstokes equations for a spreading viscous film. Phys Fluids 21(5):052104
Roisman IV, Berberović E, Tropea C (2009) Inertia dominated drop collisions. i. On the universal flow in the lamella. Phys Fluids 21(5):052103
Romagnoli V, Felton P, Prudhomme RK (2000) Control of drop size by rheology. In: Proceedings of the eighth international conference on liquid atomization and spray systems (ICLASS), Pasadena (CA, USA), pp 34–38

Rozhkov AN (1983) Dynamics of threads of diluted polymer solutions. J Eng Phys 45(1):768–774
Rozhkov AN, Prunet-Foch B, Vignes-Adler M (2003) Impact of drops of polymer solutions on small targets. Phys Fluids 15:2006–2019
Saidi A, Martin C, Magnin A (2010) Influence of yield stress on the fluid droplet impact control. J Non-Newton Fluid Mech 165:596–606
Saïdi A, Martin C, Magnin A (2011) Effects of surface properties on the impact process of a yield stress fluid drop. Exp Fluids 51(1):211–224
Schiaffino S, Sonin AA (1997) Molten droplet deposition and solidification at low weber numbers. Phys Fluids 9(11):3172–3187
Schümmer P, Tebel KH (1983) A new elongational rheometer for polymer solutions. J Non-Newton Fluid Mech 12:331–347
Smith MI, Bertola V (2010a) Effect of polymer additives on the wetting of impacting droplets. Phys Rev Lett 104(15)
Smith MI, Bertola V (2010b) The anti-rebound effect of flexible polymers on impacting drops. In: Proceedings of the 23rd European conference on liquid atomization and spray systems, Brno, Czech Republic, 6–8 Sept 2010
Smith MI, Bertola V (2011) Particle velocimetry inside newtonian and non-newtonian droplets impacting a hydrophobic surface. Exp Fluids 50(5):1385–1391
Smith MI, Sharp JS (2014) Origin of contact line forces during the retraction of dilute polymer solution drops. Langmuir 30:5455–5459
Stelter M (2001) Das Zerstäubungsverhalten nicht-Newtonscher Flüssigkeiten (The atomization behaviour of non-Newonian liquids - in German). Phdthesis, Friedrich-Alexander University Erlangen-Nürnberg
Stelter M, Brenn G, Yarin AL, Singh RP, Durst F (2000) Validation and application of a novel elongational device for polymer solutions. J Rheol 44:595–616
Stelter M, Brenn G, Yarin AL, Singh RP, Durst F (2002a) Investigation of the elongational behavior of polymer solutions by means of an elongational rheometer. J Rheol 46:507–527
Stelter M, Brenn G, Durst F (2002b) The influence of viscoelastic fluid properties on spray formation from flat-fan and pressure-swirl atomizers. At Sprays 12:299–327
Stow CD, Hadfield MG (1981) An experimental investigation of fluid flow resulting from the impact of a water drop with an unyielding dry surface. Proc R Soc Lond A: Math Phys Eng Sci 373(1755):419–441
Tadmor R (2011) Approaches in wetting phenomena. Soft Matter 7:1577–1580
Teske ME, Bilanin AJ (1994) Drop size scaling analysis of non-newtonian fluids. At Sprays 4:473–483
Thompson JC, Rothstein JP (2007) The atomization of viscoelastic fluids in flat-fan and hollow-cone spray nozzles. J Non-Newton Fluid Mech 147:11–22
Tirtaatmadja V, Sridhar T (1993) A filament stretching device for measurement of extensional viscosity. J. Rheol 37:1081–1102
Wachters LHJ, Westerling NAJ (1966) The heat transfer from a hot wall to impinging water drops in the spheroidal state. Chem Eng Sci 21(11):1047–1056
Wang A-B, Lin C-H, Chen C-C (2000) The critical temperature of dry impact for tiny droplet impinging on a heated surface. Phys Fluids 12(6):1622–1625
Wang Y, Minh D-Q, Amberg G (2017) Impact of viscoelastic droplets. Journal of Non-Newtonian Fluid Mechanics 243:38–46
Weber C (1931) Zum zerfall eines flssigkeitsstrahles. ZAMM—J Appl Math Mech/Zeitschrift für Angewandte Mathematik und Mechanik 11(2):136–154
Williams PA, English RJ, Blanchard RL, Rose SA, Lyons L, Whitehead M (2008) The influence of the extensional viscosity of very low concentrations of high molecular mass water-soluble polymers on atomisation and droplet impact. Pest Manag Sci 64(5):497–504
Worthington AM (1876) On the forms assumed by drops of liquids falling vertically on a horizontal plate. Proc R Soc Lond 25(171–178):261–272

Yao S-C, Cai KY (1988) The dynamics and leidenfrost temperature of drops impacting on a hot surface at small angles. Exp Therm Fluid Sci 1(4):363–371. ISSN 0894-1777

Yarin AL (1990) Strong flows of polymeric liquids. Part 1. Rheological behaviour. J Non-Newton Fluid Mech 37:113–138

Yarin AL (1993) Free liquid jets and films—hydrodynamics and rheology. Longman Sci Tech

Yarin AL (2006) Drop impact dynamics: splashing, spreading, receding, bouncing. Annu Rev Fluid Mech 38:159–192

Zhu H, Dexter RW, Fox RD, Reichard DL, Brazee RD, Ozkan HE (1997) Effects of polymer composition and viscosity on droplet size of recirculated spray solutions. J Agric Eng Res 67:35–45